Mathematics

https://www.aimspress.com/journal/Math

AIMS Mathematics, 11(3): 8762–8791.
DOI: 10.3934/math.2026360
Received: 11 January 2026
Revised: 25 March 2026
Accepted: 27 March 2026
Published: 31 March 2026

Research article

Two-dimensional numerical modeling and simulation of heat and moisture transfer during drying

Ishtiaq Ali*

Department of Mathematics and Statistics, College of Science, King Faisal University, P. O. Box 400, Al-Ahsa, 31982, Saudi Arabia

* **Correspondence:** Email: iamirzada@kfu.edu.sa.

Abstract: This study explores a two-dimensional model for transient heat and moisture transfer in a rectangular domain subject to convective boundary conditions. The governing equations consist of parabolic partial differential equations, which are derived from Fourier's law of heat conduction and Fick's law of mass diffusion. The model equations are discretized using central finite-difference approximations in space and a Crank–Nicolson (CN) scheme in time. To efficiently handle the multidimensional diffusion operators, an operator splitting strategy based on the Peaceman–Rachford alternating direction implicit (ADI) method is employed. This approach decomposes the two-dimensional diffusion operator into a sequence of one-dimensional subproblems, each associated with a single spatial direction, which significantly reduces the computational complexity of the fully implicit scheme while retaining second-order accuracy in time and space and unconditional stability for linear diffusion operators. The numerical scheme is shown to be unconditionally stable for the diffusion operators and computationally efficient for long-time simulations. The numerical results for the temperature and moisture fields are validated through comparison with available analytical solutions and experimental data from the literature, demonstrating very good agreement in all cases. In addition, a structure-preserving iteration method (SPIM) applied to the unsplit CN formulation is used as a benchmark reference, confirming that the proposed ADI–CN splitting achieves accuracy comparable to the unsplit CN scheme while maintaining competitive computational efficiency.

Keywords: heat and moisture transfer; parabolic partial differential equations; operator splitting strategy; numerical simulations
Mathematics Subject Classification: 35K05, 80M20, 65M22

1. Introduction

Drying is one of the oldest and most widely used techniques for food preservation and material stabilization, and it is extensively applied in biotechnology, ceramics, wood processing, and agriculture. In developed countries, drying accounts for approximately 10%–25% of total industrial energy consumption [1]. Optimizing drying operations is essential for both economic efficiency and environmental sustainability, as drying processes are widely employed across multiple industries and account for substantial energy consumption. Drying is the process of removing moisture from wet materials through evaporation. It also involves simultaneous heat and mass transfer. The drying kinetics and the ultimate quality of food and biomaterials are governed by the simultaneous inward conduction of heat and outward diffusion of moisture. One of the main challenges in drying food materials is that they often shrink during the drying process. This is particularly important when optimizing drying systems, since heat and moisture transport interact strongly within the material. In convective drying, the hot air moves heat from the wet product to the solid matrix, which increases the temperature of both the solid matrix and the surrounding air. The water moves toward the surface, evaporates, and then spreads out into the air as vapor. The air velocity and temperature strongly influence the rates of heat and mass transfer. Moisture migrates toward the surface, where it evaporates and diffuses into the surrounding air as vapor. The vapor pressure in the air around it goes down when the temperature rises, but the vapor pressure inside the wet solid goes up. This facilitates the movement of water from regions of elevated vapor pressure to regions of diminished vapor pressure [2].

The drying process in porous materials can be described mathematically using a set of coupled partial differential equations that control the flow of heat and moisture. The temperature and moisture fields are strongly coupled because heat conduction and moisture diffusion occur simultaneously. The temperature and humidity of the area can also change the material's properties, such as thermal conductivity and diffusivity. This significantly increases the complexity of the mathematical model. While using two-dimensional representations, one has to think about spatial gradients in more than one direction because real things are three-dimensional. The removal of moisture from dense products does not occur uniformly throughout the material. Accurate prediction of moisture distribution within the product, therefore, requires two- or three-dimensional models rather than surface-based approximations. In the initial stages of numerical study, researchers frequently employed explicit finite-difference approaches. These approaches required minimal temporal increments to maintain stability, analogous to the CFL requirement [3].

A comprehensive experimental and theoretical investigation has been undertaken to clarify these issues. Chiang and Petersen investigated how the moisture and temperature changed over time during the drying process of apples to support their theoretical models [4]. In theory, analytical solutions can only be found for simple configurations. Consequently, numerical methods are essential for solving such problems and for accurately predicting the evolution of temperature and moisture fields during the drying process. Many studies have created models for drying processes that use Fourier's equation of heat conduction and Fick's rule of moisture diffusion [5]. With the advancement of computational resources and numerical methods, more sophisticated drying models have been developed. Hussain and Dincer employed a precise finite-difference method to create a two-dimensional simulation of the movement of heat and moisture during the drying process of rectangular objects [6, 7]. These studies showed how important it is to deal with differences in the product area, even though strict stability standards make things harder. Drying simulations have come a long way in the last 20 years. Advanced models consider how internal pressure changes, how materials shrink, how diffusion is directed, and how things change shape when they are under stress. Ruiz-Cabrera and his team studied how moisture diffusion changed the way carrots dried. This shows how important it is to get exact measurements of how moisture spreads [8]. Akiyama et al. created a model for heat and moisture that shows how too much moisture stress can cause cracks to form [9]. Rogers and Kaviany examined the transport of heat and mass through beds of fine particles [10]. Perré et al. examined the drying processes of concrete and softwood at elevated temperatures via convection, employing one- and two-dimensional models [11]. Sun and Marrero conducted experiments to determine the convective transfer coefficients for the drying of porous cylinders [12]. Dincer and Dost created analytical models to determine the rate at which moisture disseminates through various geometries [13].

Villa-Corrales et al. used both two-dimensional numerical modeling and real-world testing to investigate mango drying [14]. A recent study utilized multiphysics coupling to investigate the interaction between stress and strain, along with the morphological changes of the material during the drying process [15]. The finite difference and finite volume methods are widely used to model heat and mass transfer in drying processes [16–18]. Advanced numerical and computational fluid dynamics-based algorithms have been applied to simulate coupled heat and mass circulation during drying processes, such as microwave and freeze-drying applications [19–21]. Numerical and experimental studies have extensively investigated time-dependent and nonlinear heat and mass transfer in drying of porous materials [22–24]. Jayapragasam et al. added complex eigenvalues to Luikov-type analytical frameworks [25]. Sychevskii studied how heat and mass move in systems that are used to dry wood [26]. Yang et al. developed a numerical solution with a very accurate way to solve two-dimensional mass transport problems in food engineering [27]. Numerous modeling approaches have been developed to estimate effective moisture diffusivity from drying data [28].

This study improves previous research on two-dimensional coupled heat and mass transfer models for rectangular geometries by incorporating several methodological advancements. We employ the Peaceman–Rachford alternating direction implicit (ADI) approach in conjunction with Crank–Nicolson (CN) time discretization. This approach is efficient and accurate to the second order in both spatial and temporal dimensions. A temporally updated coupling mechanism is employed within the ADI framework to address the variations in moisture diffusivity with temperature. This maintains the linear subproblem framework and computational efficiency. Analytical solutions exist for simple instances with constant coefficients; however, the present model incorporates temperature-dependent diffusivity and heat-mass interaction, which lack a closed-form solution. Analytical solutions are mostly employed to verify the accuracy of benchmark solutions. We verify the precision of the numerical framework by comparing it with analytical solutions and experimental data available in the literature. The methodology for simulating the two-dimensional heat and moisture movement during convective drying has shown good agreement with both analytical and experimental results.

The remainder of this paper is organized as follows. Section 2 presents the governing equations, nondimensional formulation, and detailed description of the numerical schemes. Section 3 discusses the numerical results. Section 4 concludes the paper.

2. Mathematical modeling of heat and moisture transfer

The mathematical analysis of the convective drying process is based on Fourier's law of heat conduction and Fick's law of mass diffusion. Owing to the strong analogy between heat and mass transfer, the governing Fickian diffusion equation for moisture transport takes the same mathematical form as the Fourier heat conduction equation, with temperature and thermal diffusivity replaced by moisture content and moisture diffusivity, respectively. Throughout the analysis, we consider several assumptions. First, we assume that the thermophysical properties of the solid are constant. Second, we assume that the object does not shrink or deform significantly during drying. Third, we assume that the material does not generate heat internally. Fourth, we assume the drying-air temperature remains constant throughout the process. Finally, we assume that heat and moisture move in two dimensions within a rectangular solid. In the present model, we assume a fixed geometry and neglect volumetric shrinkage during drying. This approximation is appropriate for relatively rigid porous materials or drying conditions in which geometric modifications are not significant in terms of the characteristic dimensions.

The computational domain is a two-dimensional rectangular region defined as

$$\Omega = \left\{(\mathrm{u}, \mathrm{v}) \,\middle|\, 0 \le \mathrm{u} \le \mathcal{L},\ 0 \le \mathrm{v} \le \mathcal{H}\right\},$$

where $\mathcal{L}$ and $\mathcal{H}$ denote the length and height of the object, respectively. The transient temperature distribution $\mathcal{T}(\mathrm{u}, \mathrm{v}, \mathrm{t})$ inside the solid is governed by the two-dimensional heat conduction equation,

$$\frac{\partial \mathcal{T}}{\partial \mathrm{t}} = \alpha \left(\frac{\partial^2 \mathcal{T}}{\partial \mathrm{u}^2} + \frac{\partial^2 \mathcal{T}}{\partial \mathrm{v}^2} \right), \tag{2.1}$$

where $\alpha = k/(\rho c_p)$ denotes the thermal diffusivity of the material, with k being the thermal conductivity, ρ the density, and c_p the specific heat. The initial temperature of the object is assumed uniform:

$$\mathcal{T}(\mathrm{u}, \mathrm{v}, 0) = \mathcal{T}_i, \qquad (\mathrm{u}, \mathrm{v}) \in \Omega. \tag{2.2}$$

Convective (Robin-type) boundary conditions are imposed on all external surfaces. At the vertical boundaries,

$$-k \frac{\partial \mathcal{T}}{\partial \mathrm{u}}\bigg|_{\mathrm{u}=0} = h(\mathcal{T}(0, \mathrm{v}, \mathrm{t}) - \mathcal{T}_d), \tag{2.3}$$

$$-k \frac{\partial \mathcal{T}}{\partial \mathrm{u}}\bigg|_{\mathrm{u}=\mathcal{L}} = h(\mathcal{T}(\mathcal{L}, \mathrm{v}, \mathrm{t}) - \mathcal{T}_d), \tag{2.4}$$

and at the horizontal boundaries,

$$-k \frac{\partial \mathcal{T}}{\partial \mathrm{v}}\bigg|_{\mathrm{v}=0} = h(\mathcal{T}(\mathrm{u}, 0, \mathrm{t}) - \mathcal{T}_d), \tag{2.5}$$

$$-k \frac{\partial \mathcal{T}}{\partial \mathrm{v}}\bigg|_{\mathrm{v}=\mathcal{H}} = h(\mathcal{T}(\mathrm{u}, \mathcal{H}, \mathrm{t}) - \mathcal{T}_d), \tag{2.6}$$

where h is the convective heat transfer coefficient and $\mathcal{T}_d$ denotes the drying-air temperature.

Similarly, for the moisture transfer model, the transient moisture distribution $\mathcal{M}(\mathrm{u}, \mathrm{v}, \mathrm{t})$ inside the solid is described by the two-dimensional diffusion equation,

$$\frac{\partial \mathcal{M}}{\partial \mathrm{t}} = \mathcal{D}(\mathrm{t}) \left(\frac{\partial^2 \mathcal{M}}{\partial \mathrm{u}^2} + \frac{\partial^2 \mathcal{M}}{\partial \mathrm{v}^2} \right), \tag{2.7}$$

where $\mathcal{D}(\mathrm{t})$ denotes the effective moisture diffusivity.

The initial moisture content is assumed spatially uniform:

$$\mathcal{M}(\mathrm{u}, \mathrm{v}, 0) = \mathcal{M}_i, \qquad (\mathrm{u}, \mathrm{v}) \in \Omega. \tag{2.8}$$

Convective mass transfer boundary conditions are prescribed on all boundaries. At $\mathrm{u} = 0$ and $\mathrm{u} = \mathcal{L}$,

$$-\mathcal{D}(\mathrm{t}) \frac{\partial \mathcal{M}}{\partial \mathrm{u}} \bigg|_{\mathrm{u}=0} = h_m(\mathcal{M}(0, \mathrm{v}, \mathrm{t}) - \mathcal{M}_d), \tag{2.9}$$

$$-\mathcal{D}(\mathrm{t}) \frac{\partial \mathcal{M}}{\partial \mathrm{u}} \bigg|_{\mathrm{u}=\mathcal{L}} = h_m(\mathcal{M}(\mathcal{L}, \mathrm{v}, \mathrm{t}) - \mathcal{M}_d), \tag{2.10}$$

and at $\mathrm{v} = 0$ and $\mathrm{v} = \mathcal{H}$,

$$-\mathcal{D}(\mathrm{t}) \frac{\partial \mathcal{M}}{\partial \mathrm{v}} \bigg|_{\mathrm{v}=0} = h_m(\mathcal{M}(\mathrm{u}, 0, \mathrm{t}) - \mathcal{M}_d), \tag{2.11}$$

$$-\mathcal{D}(\mathrm{t}) \frac{\partial \mathcal{M}}{\partial \mathrm{v}} \bigg|_{\mathrm{v}=\mathcal{H}} = h_m(\mathcal{M}(\mathrm{u}, \mathcal{H}, \mathrm{t}) - \mathcal{M}_d), \tag{2.12}$$

where h_m is the convective mass transfer coefficient and $\mathcal{M}_d$ denotes the equilibrium moisture content at the drying surface.

The moisture diffusivity is assumed to depend on temperature according to an Arrhenius-type relation:

$$\mathcal{D}(\mathrm{u}, \mathrm{v}, \mathrm{t}) = \mathcal{D}_0 \exp\left(-\frac{E_a}{R\mathcal{T}(\mathrm{u}, \mathrm{v}, \mathrm{t})} \right), \tag{2.13}$$

where $\mathcal{D}_0$ is the pre-exponential factor, E_a denotes the activation energy, and R is the universal gas constant. Such an Arrhenius-type temperature dependence of effective moisture diffusivity is widely adopted in drying literature to describe thermally activated moisture transport in food materials [28].

In the present study, the ratio E_a/R is taken as 1119 K, which lies within the range of reported activation parameters for food materials. In the numerical implementation, in order to preserve the linear ADI structure and computational efficiency, the diffusivity is evaluated using the spatially averaged temperature at each time level. Consequently, the coefficient is treated as time-dependent only, i.e.,

$$\mathcal{D}(\mathrm{t}) = \mathcal{D}_0 \exp\left(-\frac{1119}{\overline{\mathcal{T}}(\mathrm{t})} \right),$$

and is held constant within each time step. This averaging strategy avoids introducing a strongly space-dependent coefficient into the moisture equation at each time level, which would otherwise destroy the standard ADI line-solver structure. Consequently, within each time step the coefficient is updated sequentially from the computed temperature field, keeping the moisture subproblem linear at each time level and enabling an efficient ADI-CN implementation. Moreover, although the Arrhenius law is inherently space–time dependent through $\mathcal{T}(\mathrm{u},\mathrm{v},\mathrm{t})$, the use of $\overline{\mathcal{T}}(\mathrm{t})$ yields a time-dependent coefficient $\mathcal{D}(\mathrm{t})$, which preserves the ADI line-solver structure and enables a fair comparison with constant-coefficient analytical solutions.

The governing equations are nondimensionalized to reduce the number of governing parameters and to obtain a formulation suitable for systematic numerical analysis. For this purpose, we introduce the dimensionless relation.

$$\bar{\mathrm{u}} = \frac{\mathrm{u}}{\mathcal{L}}, \qquad \bar{\mathrm{v}} = \frac{\mathrm{v}}{\mathcal{H}}, \qquad \bar{\mathrm{t}} = \frac{\alpha\,\mathrm{t}}{\mathcal{L}^2}, \qquad \lambda = \frac{\mathcal{L}}{\mathcal{H}}. \tag{2.14}$$

Then $\mathrm{u} = \mathcal{L}\bar{\mathrm{u}}$, $\mathrm{v} = \mathcal{H}\bar{\mathrm{v}}$, and

$$(\bar{\mathrm{u}}, \bar{\mathrm{v}}) \in [0,1] \times [0,1].$$

Moreover, from $\bar{\mathrm{t}} = \alpha\,\mathrm{t}/\mathcal{L}^2$, we have

$$\mathrm{t} = \frac{\mathcal{L}^2}{\alpha}\bar{\mathrm{t}}, \qquad \frac{\partial}{\partial \mathrm{t}} = \frac{\alpha}{\mathcal{L}^2}\frac{\partial}{\partial \bar{\mathrm{t}}}.$$

Define the dimensionless temperature and moisture fields by

$$\mathcal{T}^*(\bar{\mathrm{u}}, \bar{\mathrm{v}}, \bar{\mathrm{t}}) = \frac{\mathcal{T}(\mathrm{u},\mathrm{v},\mathrm{t}) - \mathcal{T}_i}{\mathcal{T}_d - \mathcal{T}_i}, \qquad \mathcal{M}^*(\bar{\mathrm{u}}, \bar{\mathrm{v}}, \bar{\mathrm{t}}) = \frac{\mathcal{M}(\mathrm{u},\mathrm{v},\mathrm{t}) - \mathcal{M}_d}{\mathcal{M}_i - \mathcal{M}_d}. \tag{2.15}$$

Equivalently,

$$\mathcal{T} = \mathcal{T}_i + (\mathcal{T}_d - \mathcal{T}_i)\mathcal{T}^*, \qquad \mathcal{M} = \mathcal{M}_d + (\mathcal{M}_i - \mathcal{M}_d)\mathcal{M}^*.$$

Using $\mathrm{u} = \mathcal{L}\bar{\mathrm{u}}$ and $\mathrm{v} = \mathcal{H}\bar{\mathrm{v}}$, the chain rule gives

$$\frac{\partial}{\partial \mathrm{u}} = \frac{1}{\mathcal{L}}\frac{\partial}{\partial \bar{\mathrm{u}}}, \qquad \frac{\partial}{\partial \mathrm{v}} = \frac{1}{\mathcal{H}}\frac{\partial}{\partial \bar{\mathrm{v}}},$$

and hence

$$\frac{\partial^2}{\partial \mathrm{u}^2} = \frac{1}{\mathcal{L}^2}\frac{\partial^2}{\partial \bar{\mathrm{u}}^2}, \qquad \frac{\partial^2}{\partial \mathrm{v}^2} = \frac{1}{\mathcal{H}^2}\frac{\partial^2}{\partial \bar{\mathrm{v}}^2} = \frac{\lambda^2}{\mathcal{L}^2}\frac{\partial^2}{\partial \bar{\mathrm{v}}^2}.$$

As $\lambda = \mathcal{L}/\mathcal{H}$ implies $1/\mathcal{H}^2 = \lambda^2/\mathcal{L}^2$.

Substitute $\mathcal{T} = \mathcal{T}_i + (\mathcal{T}_d - \mathcal{T}_i)\mathcal{T}^*$ and the above derivative relations into (2.1):

$$\frac{\partial}{\partial \mathrm{t}}\Big(\mathcal{T}_i + (\mathcal{T}_d - \mathcal{T}_i)\mathcal{T}^*\Big) = \alpha\left(\frac{\partial^2}{\partial \mathrm{u}^2}\Big(\mathcal{T}_i + (\mathcal{T}_d - \mathcal{T}_i)\mathcal{T}^*\Big) + \frac{\partial^2}{\partial \mathrm{v}^2}\Big(\mathcal{T}_i + (\mathcal{T}_d - \mathcal{T}_i)\mathcal{T}^*\Big)\right).$$

Since $\mathcal{T}_i$ is constant, it vanishes under derivatives, and the factor $(\mathcal{T}_d - \mathcal{T}_i)$ cancels from both sides. Using $\partial/\partial \mathrm{t} = (\alpha/\mathcal{L}^2)\,\partial/\partial \bar{\mathrm{t}}$ and the second-derivative relations yields

$$\frac{\alpha}{\mathcal{L}^2}\frac{\partial \mathcal{T}^*}{\partial \bar{\mathrm{t}}} = \alpha\left(\frac{1}{\mathcal{L}^2}\frac{\partial^2 \mathcal{T}^*}{\partial \bar{\mathrm{u}}^2} + \frac{\lambda^2}{\mathcal{L}^2}\frac{\partial^2 \mathcal{T}^*}{\partial \bar{\mathrm{v}}^2}\right).$$

Multiplying by $\mathcal{L}^2/\alpha$ gives the dimensionless heat equation

$$\frac{\partial \mathcal{T}^*}{\partial \bar{\mathrm{t}}} = \frac{\partial^2 \mathcal{T}^*}{\partial \bar{\mathrm{u}}^2} + \lambda^2\frac{\partial^2 \mathcal{T}^*}{\partial \bar{\mathrm{v}}^2}, \qquad 0 < \bar{\mathrm{u}} < 1,\ 0 < \bar{\mathrm{v}} < 1,\ \bar{\mathrm{t}} > 0. \tag{2.16}$$

From (2.2), $\mathcal{T}(\mathrm{u},\mathrm{v},0)=\mathcal{T}_i$ implies

$$\mathcal{T}^*(\bar{\mathrm{u}},\bar{\mathrm{v}},0)=\frac{\mathcal{T}_i-\mathcal{T}_i}{\mathcal{T}_d-\mathcal{T}_i}=0,$$

hence

$$\mathcal{T}^*(\bar{\mathrm{u}},\bar{\mathrm{v}},0)=0. \tag{2.17}$$

Consider the boundary at $\mathrm{u}=0$ (the same steps apply at $\mathrm{u}=\mathcal{L}$). From (2.3),

$$-k\frac{\partial\mathcal{T}}{\partial \mathrm{u}}\bigg|_{\mathrm{u}=0}=h(\mathcal{T}(0,\mathrm{v},\mathrm{t})-\mathcal{T}_d).$$

Using $\mathcal{T}=\mathcal{T}_i+(\mathcal{T}_d-\mathcal{T}_i)\mathcal{T}^*$ and $\partial/\partial\mathrm{u}=(1/\mathcal{L})\,\partial/\partial\bar{\mathrm{u}}$, we obtain

$$-k\,\frac{\mathcal{T}_d-\mathcal{T}_i}{\mathcal{L}}\frac{\partial\mathcal{T}^*}{\partial\bar{\mathrm{u}}}\bigg|_{\bar{\mathrm{u}}=0}=h\Big(\mathcal{T}_i+(\mathcal{T}_d-\mathcal{T}_i)\mathcal{T}^*-\mathcal{T}_d\Big).$$

Cancelling $(\mathcal{T}_d-\mathcal{T}_i)$ gives

$$-\frac{k}{\mathcal{L}}\frac{\partial\mathcal{T}^*}{\partial\bar{\mathrm{u}}}\bigg|_{\bar{\mathrm{u}}=0}=h(\mathcal{T}^*-1),$$

or equivalently

$$-\frac{\partial\mathcal{T}^*}{\partial\bar{\mathrm{u}}}\bigg|_{\bar{\mathrm{u}}=0}=\frac{h\mathcal{L}}{k}(\mathcal{T}^*-1).$$

Defining the Biot number in the $\bar{\mathrm{u}}$-direction by $\mathcal{B}_{\mathrm{u}}^{(\mathcal{T})}=h\mathcal{L}/k$ yields

$$-\frac{\partial\mathcal{T}^*}{\partial\bar{\mathrm{u}}}\bigg|_{\bar{\mathrm{u}}=0,1}=\mathcal{B}_{\mathrm{u}}^{(\mathcal{T})}(\mathcal{T}^*-1),\qquad \mathcal{B}_{\mathrm{u}}^{(\mathcal{T})}=\frac{h\mathcal{L}}{k}. \tag{2.18}$$

Similarly, applying the same steps to (2.5)–(2.6) and using $\partial/\partial\mathrm{v}=(1/\mathcal{H})\,\partial/\partial\bar{\mathrm{v}}$ give

$$-\frac{\partial\mathcal{T}^*}{\partial\bar{\mathrm{v}}}\bigg|_{\bar{\mathrm{v}}=0,1}=\mathcal{B}_{\mathrm{v}}^{(\mathcal{T})}(\mathcal{T}^*-1),\qquad \mathcal{B}_{\mathrm{v}}^{(\mathcal{T})}=\frac{h\mathcal{H}}{k}. \tag{2.19}$$

Using the same strategy as for the heat equation, we substitute the scalings in (2.14)–(2.15) into the dimensional moisture model (2.7). In particular, $\partial/\partial\mathrm{t}=(\alpha/\mathcal{L}^2)\,\partial/\partial\bar{\mathrm{t}}$, $\partial^2/\partial\mathrm{u}^2=(1/\mathcal{L}^2)\,\partial^2/\partial\bar{\mathrm{u}}^2$, and $\partial^2/\partial\mathrm{v}^2=(1/\mathcal{H}^2)\,\partial^2/\partial\bar{\mathrm{v}}^2=(\lambda^2/\mathcal{L}^2)\,\partial^2/\partial\bar{\mathrm{v}}^2$. Moreover, from $\mathcal{M}=\mathcal{M}_d+(\mathcal{M}_i-\mathcal{M}_d)\mathcal{M}^*$, the factor $(\mathcal{M}_i-\mathcal{M}_d)$ cancels out after differentiation. Therefore, (2.7) reduces to the dimensionless form

$$\frac{\partial\mathcal{M}^*}{\partial\bar{\mathrm{t}}}=\mathcal{G}(\bar{\mathrm{t}})\left(\frac{\partial^2\mathcal{M}^*}{\partial\bar{\mathrm{u}}^2}+\lambda^2\frac{\partial^2\mathcal{M}^*}{\partial\bar{\mathrm{v}}^2}\right),\qquad 0<\bar{\mathrm{u}}<1,\ 0<\bar{\mathrm{v}}<1,\ \bar{\mathrm{t}}>0, \tag{2.20}$$

where the dimensionless diffusivity ratio is defined by

$$\mathcal{G}(\bar{\mathrm{t}})=\frac{\mathcal{D}(\mathrm{t})}{\alpha}. \tag{2.21}$$

From the initial condition $\mathcal{M}(\mathrm{u},\mathrm{v},0)=\mathcal{M}_i$ in (2.8), we directly obtain

$$\mathcal{M}^*(\bar{\mathrm{u}},\bar{\mathrm{v}},0)=1. \tag{2.22}$$

Next, consider the convective (Robin) moisture boundary condition in the normal direction, $-\mathcal{D}(\mathrm{t})\,\partial\mathcal{M}/\partial n = h_m(\mathcal{M}-\mathcal{M}_d)$. Using $\partial/\partial\mathrm{u} = (1/\mathcal{L})\,\partial/\partial\bar{\mathrm{u}}$ and $\mathcal{M}-\mathcal{M}_d = (\mathcal{M}_i-\mathcal{M}_d)\mathcal{M}^*$, the common factor $(\mathcal{M}_i - \mathcal{M}_d)$ cancels, which yields

$$-\frac{\partial\mathcal{M}^*}{\partial\bar{\mathrm{u}}}\bigg|_{\bar{\mathrm{u}}=0} = \mathcal{B}_{\mathrm{u}}^{(\mathcal{M})}(\mathrm{t})\,\mathcal{M}^*, \qquad -\frac{\partial\mathcal{M}^*}{\partial\bar{\mathrm{u}}}\bigg|_{\bar{\mathrm{u}}=1} = \mathcal{B}_{\mathrm{u}}^{(\mathcal{M})}(\mathrm{t})\,\mathcal{M}^*, \tag{2.23}$$

$$-\frac{\partial\mathcal{M}^*}{\partial\bar{\mathrm{v}}}\bigg|_{\bar{\mathrm{v}}=0} = \mathcal{B}_{\mathrm{v}}^{(\mathcal{M})}(\mathrm{t})\,\mathcal{M}^*, \qquad -\frac{\partial\mathcal{M}^*}{\partial\bar{\mathrm{v}}}\bigg|_{\bar{\mathrm{v}}=1} = \mathcal{B}_{\mathrm{v}}^{(\mathcal{M})}(\mathrm{t})\,\mathcal{M}^*, \tag{2.24}$$

where the directional mass Biot numbers are

$$\mathcal{B}_{\mathrm{u}}^{(\mathcal{M})}(\mathrm{t}) = \frac{h_m\,\mathcal{L}}{\mathcal{D}(\mathrm{t})}, \qquad \mathcal{B}_{\mathrm{v}}^{(\mathcal{M})}(\mathrm{t}) = \frac{h_m\,\mathcal{H}}{\mathcal{D}(\mathrm{t})}. \tag{2.25}$$

Finally, expressing the averaged Arrhenius-type law in terms of $\mathcal{T}^*$ via $\mathcal{T} = \mathcal{T}_i + (\mathcal{T}_d - \mathcal{T}_i)\mathcal{T}^*$ yields

$$\mathcal{D}(\mathrm{t}) = \mathcal{D}_0\exp\left(-\frac{1119}{\mathcal{T}_i + (\mathcal{T}_d-\mathcal{T}_i)\,\overline{\mathcal{T}^*}(\bar{\mathrm{t}})}\right), \tag{2.26}$$

where the dimensionless spatial average is defined by

$$\overline{\mathcal{T}^*}(\bar{\mathrm{t}}) = \int_0^1\int_0^1 \mathcal{T}^*(\bar{\mathrm{u}},\bar{\mathrm{v}},\bar{\mathrm{t}})\,\mathrm{d}\bar{\mathrm{u}}\,\mathrm{d}\bar{\mathrm{v}}. \tag{2.27}$$

For completeness, the corresponding dimensionally averaged temperature used in the Arrhenius update satisfies

$$\overline{\mathcal{T}}(\mathrm{t}) = \mathcal{T}_i + (\mathcal{T}_d - \mathcal{T}_i)\,\overline{\mathcal{T}^*}(\bar{\mathrm{t}}).$$

Consequently, within each time step, the coefficient $\mathcal{G}(\bar{\mathrm{t}}) = \mathcal{D}(\mathrm{t})/\alpha$ in (2.20) is treated as constant and is updated sequentially from the computed temperature field, keeping the moisture subproblem linear at each time level and enabling an efficient ADI–CN implementation.

2.1. Description of numerical scheme

Let the dimensionless domain be

$$\bar{\Omega} = [0,1]\times[0,1], \qquad \bar{\mathrm{u}} = \mathrm{u}/\mathcal{L}, \qquad \bar{\mathrm{v}} = \mathrm{v}/\mathcal{H}, \qquad \bar{\mathrm{t}} = \alpha\,\mathrm{t}/\mathcal{L}^2.$$

We introduce the uniform spatial grids

$$\bar{\mathrm{u}}_i = i\,\Delta\bar{\mathrm{u}}, \quad i = 0,1,\ldots,\mathcal{N}_{\mathrm{u}}, \qquad \bar{\mathrm{v}}_j = j\,\Delta\bar{\mathrm{v}}, \quad j = 0,1,\ldots,\mathcal{N}_{\mathrm{v}},$$

with

$$\Delta\bar{\mathrm{u}} = \frac{1}{\mathcal{N}_{\mathrm{u}}}, \qquad \Delta\bar{\mathrm{v}} = \frac{1}{\mathcal{N}_{\mathrm{v}}},$$

and the time levels

$$\bar{\mathrm{t}}^n = n\,\Delta\bar{\mathrm{t}}, \qquad n = 0,1,2,\ldots.$$

The grid approximations are denoted by

$$\mathcal{T}^{*,n}_{i,j} \approx \mathcal{T}^*(\bar{\mathrm{u}}_i,\bar{\mathrm{v}}_j,\bar{\mathrm{t}}^n), \qquad \mathcal{M}^{*,n}_{i,j} \approx \mathcal{M}^*(\bar{\mathrm{u}}_i,\bar{\mathrm{v}}_j,\bar{\mathrm{t}}^n),$$

and we write

$$\lambda = \frac{\mathcal{L}}{\mathcal{H}}.$$

The Robin boundary conditions in (2.18)–(2.19) and (2.23)–(2.24) are enforced by ghost-point elimination. For the heat equation, define

$$C_{\mathcal{T},\mathrm{u}} = \mathcal{B}_{\mathrm{u}}^{(\mathcal{T})}\,\Delta\bar{\mathrm{u}}, \qquad C_{\mathcal{T},\mathrm{v}} = \mathcal{B}_{\mathrm{v}}^{(\mathcal{T})}\,\Delta\bar{\mathrm{v}}. \tag{2.28}$$

Then the boundary nodal values satisfy

$$\mathcal{T}_b^* = \frac{\mathcal{T}_{\mathrm{in}}^* + C_{\mathcal{T}}}{1 + C_{\mathcal{T}}}, \qquad C_{\mathcal{T}} \in \{C_{\mathcal{T},\mathrm{u}}, C_{\mathcal{T},\mathrm{v}}\}, \tag{2.29}$$

since the surrounding air corresponds to the dimensionless equilibrium state $\mathcal{T}^* = 1$.

At time level $\bar{\mathrm{t}}^n$, define the moisture boundary parameters

$$C_{\mathcal{M},\mathrm{u}}^n = \mathcal{B}_{\mathrm{u}}^{(\mathcal{M})}(\bar{\mathrm{t}}^n)\,\Delta\bar{\mathrm{u}}, \qquad C_{\mathcal{M},\mathrm{v}}^n = \mathcal{B}_{\mathrm{v}}^{(\mathcal{M})}(\bar{\mathrm{t}}^n)\,\Delta\bar{\mathrm{v}}. \tag{2.30}$$

Then the moisture boundary nodal values satisfy

$$\mathcal{M}_b^* = \frac{\mathcal{M}_{\mathrm{in}}^*}{1 + C_{\mathcal{M}}^n}, \qquad C_{\mathcal{M}}^n \in \{C_{\mathcal{M},\mathrm{u}}^n, C_{\mathcal{M},\mathrm{v}}^n\}. \tag{2.31}$$

Since

$$\mathcal{M}^* = \frac{\mathcal{M} - \mathcal{M}_d}{\mathcal{M}_i - \mathcal{M}_d}.$$

The equilibrium boundary state for the moisture variable is: $\mathcal{M}^* = 0$, even when $\mathcal{M}_d \neq 0$ in dimensional form.

For the heat equation (2.16), define

$$\nabla_{\mathrm{u}}^{(\mathcal{T})} = \frac{\Delta\bar{\mathrm{t}}}{2(\Delta\bar{\mathrm{u}})^2}, \qquad \nabla_{\mathrm{v}}^{(\mathcal{T})} = \frac{\lambda^2\,\Delta\bar{\mathrm{t}}}{2(\Delta\bar{\mathrm{v}})^2}. \tag{2.32}$$

For the moisture equation (2.20), the diffusivity ratio

$$\mathcal{G}(\bar{\mathrm{t}}) = \frac{\mathcal{D}(\mathrm{t})}{\alpha}$$

depends on the temperature field and is therefore time-dependent. To preserve the linear structure of the ADI–CN scheme, we adopt a frozen-coefficient approach. After computing $\mathcal{T}^{*,n}$, we form the spatial average

$$\overline{\mathcal{T}^*}(\bar{\mathrm{t}}^n) = \int_0^1\int_0^1 \mathcal{T}^*(\bar{\mathrm{u}},\bar{\mathrm{v}},\bar{\mathrm{t}}^n)\,d\bar{\mathrm{u}}\,d\bar{\mathrm{v}},$$

and update the dimensional diffusivity.

$$\mathcal{D}^n = \mathcal{D}_0\exp\!\left(-\frac{1119}{\mathcal{T}_i + (\mathcal{T}_d - \mathcal{T}_i)\,\overline{\mathcal{T}^*}(\bar{\mathrm{t}}^n)}\right), \qquad \mathcal{G}^n = \frac{\mathcal{D}^n}{\alpha}.$$

The coefficient $\mathcal{G}(\bar{\mathrm{t}})$ is then approximated as piecewise constant over the interval.

$$\bar{\mathrm{t}} \in [\bar{\mathrm{t}}^n, \bar{\mathrm{t}}^{n+1}], \qquad \mathcal{G}(\bar{\mathrm{t}}) \approx \mathcal{G}^n.$$

Accordingly, we set

$$\nabla_{\mathrm{u}}^{(\mathcal{M})}(n) = \frac{\mathcal{G}^n\,\Delta\bar{\mathrm{t}}}{2(\Delta\bar{\mathrm{u}})^2}, \qquad \nabla_{\mathrm{v}}^{(\mathcal{M})}(n) = \frac{\mathcal{G}^n\,\lambda^2\,\Delta\bar{\mathrm{t}}}{2(\Delta\bar{\mathrm{v}})^2}. \tag{2.33}$$

For simplicity within the n-th time step, we write

$$\nabla_{\mathrm{u}}^{(\mathcal{M})} = \nabla_{\mathrm{u}}^{(\mathcal{M})}(n), \qquad \nabla_{\mathrm{v}}^{(\mathcal{M})} = \nabla_{\mathrm{v}}^{(\mathcal{M})}(n),$$

and treat these quantities as constants during the two moisture half-steps.

We now describe the ADI–CN discretization. Given $\mathcal{T}^{*,n}$, the temperature field is advanced through two half-steps. For each fixed $j = 1, 2, \ldots, \mathcal{N}_{\mathrm{v}} - 1$, solve for $\{\mathcal{T}_{i,j}^{*,n+\frac{1}{2}}\}_{i=1}^{\mathcal{N}_{\mathrm{u}}-1}$ from

$$\left(1 + 2\nabla_{\mathrm{u}}^{(\mathcal{T})}\right)\mathcal{T}_{i,j}^{*,n+\frac{1}{2}} - \nabla_{\mathrm{u}}^{(\mathcal{T})}\mathcal{T}_{i-1,j}^{*,n+\frac{1}{2}} - \nabla_{\mathrm{u}}^{(\mathcal{T})}\mathcal{T}_{i+1,j}^{*,n+\frac{1}{2}} = \left(1 - 2\nabla_{\mathrm{v}}^{(\mathcal{T})}\right)\mathcal{T}_{i,j}^{*,n} + \nabla_{\mathrm{v}}^{(\mathcal{T})}\left(\mathcal{T}_{i,j-1}^{*,n} + \mathcal{T}_{i,j+1}^{*,n}\right), \tag{2.34}$$

for $i = 1, \ldots, \mathcal{N}_{\mathrm{u}} - 1$, together with the boundary values obtained from (2.29). Because Eq (2.29) is nonhomogeneous, its substitution into the first and last interior equations introduces additional constant contributions. Therefore, the reduced line system for the heat half-step must be written as

$$\mathbf{A}_{\mathrm{u}}^{(\mathcal{T})}\,\mathbf{T}_j^{n+\frac{1}{2}} = \mathbf{b}_j^{(\mathcal{T},1)} + \mathbf{r}_j^{(\mathcal{T},1)}, \tag{2.35}$$

where $\mathbf{T}_j^{n+\frac{1}{2}} \in \mathbb{R}^{\mathcal{N}_{\mathrm{u}}-1}$ is the interior temperature vector along the j-th horizontal line, $\mathbf{b}_j^{(\mathcal{T},1)}$ collects the standard right-hand-side terms from (2.34), and $\mathbf{r}_j^{(\mathcal{T},1)}$ collects the constant boundary contributions induced by the nonhomogeneous Robin condition (2.29). More precisely,

$$\mathbf{r}_j^{(\mathcal{T},1)} = \frac{\nabla_{\mathrm{u}}^{(\mathcal{T})} C_{\mathcal{T},\mathrm{u}}}{1 + C_{\mathcal{T},\mathrm{u}}}[\,1,\ 0,\ \ldots,\ 0,\ 1]^{\mathsf{T}}.$$

Equivalently, the first and last diagonal entries of $\mathbf{A}_{\mathrm{u}}^{(\mathcal{T})}$ are modified by the ghost-point elimination, while the constant vector $\mathbf{r}_j^{(\mathcal{T},1)}$ is added to the right-hand side.

After solving each horizontal line system, the boundary nodes are updated by (2.29). Next, for each fixed $i = 1, 2, \ldots, \mathcal{N}_{\mathrm{u}} - 1$, solve for $\{\mathcal{T}_{i,j}^{*,n+1}\}_{j=1}^{\mathcal{N}_{\mathrm{v}}-1}$ from

$$\left(1 + 2\nabla_{\mathrm{v}}^{(\mathcal{T})}\right)\mathcal{T}_{i,j}^{*,n+1} - \nabla_{\mathrm{v}}^{(\mathcal{T})}\mathcal{T}_{i,j-1}^{*,n+1} - \nabla_{\mathrm{v}}^{(\mathcal{T})}\mathcal{T}_{i,j+1}^{*,n+1} = \left(1 - 2\nabla_{\mathrm{u}}^{(\mathcal{T})}\right)\mathcal{T}_{i,j}^{*,n+\frac{1}{2}} + \nabla_{\mathrm{u}}^{(\mathcal{T})}\left(\mathcal{T}_{i-1,j}^{*,n+\frac{1}{2}} + \mathcal{T}_{i+1,j}^{*,n+\frac{1}{2}}\right), \tag{2.36}$$

for $j = 1, \ldots, \mathcal{N}_{\mathrm{v}} - 1$. Again, because of the nonhomogeneous Robin elimination in Eq (2.29), the corresponding reduced line system becomes

$$\mathbf{A}_{\mathrm{v}}^{(\mathcal{T})}\,\widetilde{\mathbf{T}}_i^{n+1} = \mathbf{c}_i^{(\mathcal{T},2)} + \mathbf{r}_i^{(\mathcal{T},2)}, \tag{2.37}$$

where $\widetilde{\mathbf{T}}_i^{n+1} \in \mathbb{R}^{\mathcal{N}_{\mathrm{v}}-1}$ is the interior temperature vector along the i-th vertical line, $\mathbf{c}_i^{(\mathcal{T},2)}$ is the standard right-hand side from (2.36), and

$$\mathbf{r}_i^{(\mathcal{T},2)} = \frac{\nabla_{\mathrm{v}}^{(\mathcal{T})} C_{\mathcal{T},\mathrm{v}}}{1 + C_{\mathcal{T},\mathrm{v}}}[\,1,\ 0,\ \ldots,\ 0,\ 1]^{\mathsf{T}}$$

contains the constant contributions from the top and bottom boundaries. After solving each vertical line system, the heat boundary nodes are again updated by (2.29).

We now advance the moisture field. At time level n, the coefficient $\mathcal{G}(\bar{t})$ is frozen as $\mathcal{G}^n$, and the solution is advanced from $\mathcal{M}^{*,n}$ to $\mathcal{M}^{*,n+1}$ through two ADI half-steps. For each fixed $j = 1, 2, \ldots, \mathcal{N}_{\mathrm{v}} - 1$, solve for $\{\mathcal{M}_{i,j}^{*,n+\frac{1}{2}}\}_{i=1}^{\mathcal{N}_{\mathrm{u}}-1}$ from

$$\left(1 + 2\nabla_{\mathrm{u}}^{(\mathcal{M})}\right)\mathcal{M}_{i,j}^{*,n+\frac{1}{2}} - \nabla_{\mathrm{u}}^{(\mathcal{M})}\mathcal{M}_{i-1,j}^{*,n+\frac{1}{2}} - \nabla_{\mathrm{u}}^{(\mathcal{M})}\mathcal{M}_{i+1,j}^{*,n+\frac{1}{2}} = \left(1 - 2\nabla_{\mathrm{v}}^{(\mathcal{M})}\right)\mathcal{M}_{i,j}^{*,n} + \nabla_{\mathrm{v}}^{(\mathcal{M})}\left(\mathcal{M}_{i,j-1}^{*,n} + \mathcal{M}_{i,j+1}^{*,n}\right), \tag{2.38}$$

where $\nabla_{\mathrm{u}}^{(\mathcal{M})} = \nabla_{\mathrm{u}}^{(\mathcal{M})}(n)$ and $\nabla_{\mathrm{v}}^{(\mathcal{M})} = \nabla_{\mathrm{v}}^{(\mathcal{M})}(n)$ remain fixed during the time step.

Define

$$\mathbf{M}_j^{n+\frac{1}{2}} = [\mathcal{M}_{1,j}^{*,n+\frac{1}{2}}, \mathcal{M}_{2,j}^{*,n+\frac{1}{2}}, \ldots, \mathcal{M}_{\mathcal{N}_{\mathrm{u}}-1,j}^{*,n+\frac{1}{2}}]^{\mathsf{T}} \in \mathbb{R}^{\mathcal{N}_{\mathrm{u}}-1}.$$

Let $\mathbf{b}_j^{(\mathcal{M},1)} \in \mathbb{R}^{\mathcal{N}_{\mathrm{u}}-1}$ be defined by

$$(\mathbf{b}_j^{(\mathcal{M},1)})_p = \left(1 - 2\nabla_{\mathrm{v}}^{(\mathcal{M})}\right)\mathcal{M}_{p,j}^{*,n} + \nabla_{\mathrm{v}}^{(\mathcal{M})}\left(\mathcal{M}_{p,j-1}^{*,n} + \mathcal{M}_{p,j+1}^{*,n}\right), \qquad p = 1, \ldots, \mathcal{N}_{\mathrm{u}} - 1. \tag{2.39}$$

Let $C_3^n = C_{\mathcal{M},\mathrm{u}}^n$, so that

$$\mathcal{M}_{0,j}^{*,n+\frac{1}{2}} = \frac{\mathcal{M}_{1,j}^{*,n+\frac{1}{2}}}{1 + C_3^n}, \qquad \mathcal{M}_{\mathcal{N}_{\mathrm{u}},j}^{*,n+\frac{1}{2}} = \frac{\mathcal{M}_{\mathcal{N}_{\mathrm{u}}-1,j}^{*,n+\frac{1}{2}}}{1 + C_3^n}.$$

Then the reduced line system is

$$\mathbf{A}_{\mathrm{u}}^{(\mathcal{M})}(n)\,\mathbf{M}_j^{n+\frac{1}{2}} = \mathbf{b}_j^{(\mathcal{M},1)}, \tag{2.40}$$

where $\mathbf{A}_{\mathrm{u}}^{(\mathcal{M})}(n) \in \mathbb{R}^{(\mathcal{N}_{\mathrm{u}}-1)\times(\mathcal{N}_{\mathrm{u}}-1)}$ is tridiagonal with

$$(\mathbf{A}_{\mathrm{u}}^{(\mathcal{M})}(n))_{p,q} = \begin{cases} 1 + 2\nabla_{\mathrm{u}}^{(\mathcal{M})} - \dfrac{\nabla_{\mathrm{u}}^{(\mathcal{M})}}{1 + C_3^n}, & p = q \in \{1, \mathcal{N}_{\mathrm{u}} - 1\}, \\ 1 + 2\nabla_{\mathrm{u}}^{(\mathcal{M})}, & p = q, \ \ 2 \le p \le \mathcal{N}_{\mathrm{u}} - 2, \\ -\nabla_{\mathrm{u}}^{(\mathcal{M})}, & |p - q| = 1, \\ 0, & \text{otherwise.} \end{cases}$$

Here, no additive constant appears on the right-hand side because the moisture boundary elimination (2.31) is homogeneous and the equilibrium state is $\mathcal{M}^* = 0$.

For each fixed $i = 1, 2, \ldots, \mathcal{N}_{\mathrm{u}} - 1$, solve for $\{\mathcal{M}_{i,j}^{*,n+1}\}_{j=1}^{\mathcal{N}_{\mathrm{v}}-1}$ from

$$\left(1 + 2\nabla_{\mathrm{v}}^{(\mathcal{M})}\right)\mathcal{M}_{i,j}^{*,n+1} - \nabla_{\mathrm{v}}^{(\mathcal{M})}\mathcal{M}_{i,j-1}^{*,n+1} - \nabla_{\mathrm{v}}^{(\mathcal{M})}\mathcal{M}_{i,j+1}^{*,n+1} = \left(1 - 2\nabla_{\mathrm{u}}^{(\mathcal{M})}\right)\mathcal{M}_{i,j}^{*,n+\frac{1}{2}} + \nabla_{\mathrm{u}}^{(\mathcal{M})}\left(\mathcal{M}_{i-1,j}^{*,n+\frac{1}{2}} + \mathcal{M}_{i+1,j}^{*,n+\frac{1}{2}}\right). \tag{2.41}$$

Define

$$\mathbf{M}_i^{n+1} = [\mathcal{M}_{i,1}^{*,n+1}, \mathcal{M}_{i,2}^{*,n+1}, \ldots, \mathcal{M}_{i,\mathcal{N}_{\mathrm{v}}-1}^{*,n+1}]^{\mathsf{T}} \in \mathbb{R}^{\mathcal{N}_{\mathrm{v}}-1},$$

and let $\mathbf{c}_i^{(\mathcal{M},2)} \in \mathbb{R}^{\mathcal{N}_{\mathrm{v}}-1}$ be

$$(\mathbf{c}_i^{(\mathcal{M},2)})_p = \left(1 - 2\nabla_{\mathrm{u}}^{(\mathcal{M})}\right)\mathcal{M}_{i,p}^{*,n+\frac{1}{2}} + \nabla_{\mathrm{u}}^{(\mathcal{M})}\left(\mathcal{M}_{i-1,p}^{*,n+\frac{1}{2}} + \mathcal{M}_{i+1,p}^{*,n+\frac{1}{2}}\right), \qquad p = 1, \ldots, \mathcal{N}_{\mathrm{v}} - 1. \tag{2.42}$$

Using $C_4^n = C_{\mathcal{M},\mathrm{v}}^n$, we have

$$\mathcal{M}_{i,0}^{*,n+1} = \frac{\mathcal{M}_{i,1}^{*,n+1}}{1+C_4^n}, \qquad \mathcal{M}_{i,\mathcal{N}_\mathrm{v}}^{*,n+1} = \frac{\mathcal{M}_{i,\mathcal{N}_\mathrm{v}-1}^{*,n+1}}{1+C_4^n}.$$

Hence the second moisture half-step is written as

$$\mathbf{A}_\mathrm{v}^{(\mathcal{M})}(n)\,\mathbf{M}_i^{n+1} = \mathbf{c}_i^{(\mathcal{M},2)}, \tag{2.43}$$

where $\mathbf{A}_\mathrm{v}^{(\mathcal{M})}(n) \in \mathbb{R}^{(\mathcal{N}_\mathrm{v}-1)\times(\mathcal{N}_\mathrm{v}-1)}$ is tridiagonal with

$$(\mathbf{A}_\mathrm{v}^{(\mathcal{M})}(n))_{p,q} = \begin{cases} 1+2\nabla_\mathrm{v}^{(\mathcal{M})} - \dfrac{\nabla_\mathrm{v}^{(\mathcal{M})}}{1+C_4^n}, & p=q\in\{1,\mathcal{N}_\mathrm{v}-1\}, \\ 1+2\nabla_\mathrm{v}^{(\mathcal{M})}, & p=q,\ \ 2\le p\le \mathcal{N}_\mathrm{v}-2, \\ -\nabla_\mathrm{v}^{(\mathcal{M})}, & |p-q|=1, \\ 0, & \text{otherwise}. \end{cases}$$

Again, no constant term appears on the right-hand side because the equilibrium moisture state is $\mathcal{M}^* = 0$.

At each time level n, the average temperature $\overline{\mathcal{T}^*}(\bar{t}^n)$ is first used to evaluate $\mathcal{D}^n$ and hence $\mathcal{G}^n$. The heat equation is then solved to obtain $\mathcal{T}^{*,n+1}$ from (2.35) and (2.37). Subsequently, the moisture equation is advanced from $\mathcal{M}^{*,n}$ to $\mathcal{M}^{*,n+1}$ by (2.38)–(2.43), using the frozen coefficient $\mathcal{G}^n$ over the interval $[\bar{t}^n, \bar{t}^{n+1}]$.

Each ADI line system is tridiagonal and can therefore be solved efficiently by the Thomas algorithm, leading to an overall computational complexity of $O(\mathcal{N}_\mathrm{u}\mathcal{N}_\mathrm{v})$ per time step. The time increment $\Delta\bar{t}$ is chosen mainly according to accuracy requirements, since the ADI–CN discretization is unconditionally stable for linear diffusion problems. In the present coupled problem, freezing the coefficient $\mathcal{G}$ piecewise in time preserves the ADI line-solver structure and yields an efficient sequential coupling strategy. The resulting ADI–CN framework is applicable to a broad class of two-dimensional parabolic diffusion problems whose operators admit directional splitting.

2.2. *Structure-preserving iteration method*

To further assess the efficiency and accuracy of the proposed ADI–CN scheme, we include a comparison against a SPIM that solves, at each time level, the unsplit Crank–Nicolson discretization of the same two-dimensional diffusion operators. It is important to emphasize that the SPIM employed in the present work is not a new discretization scheme for the governing partial differential equations. Instead, it serves solely as a stationary matrix-splitting solver for the linear system generated by the unsplit CN discretization.

The term structure-preserving signifies that the iteration does not modify the underlying CN discretization itself. Rather, it provides a directional stationary solver for the corresponding two-dimensional midpoint system. Since the iteration converges to the exact solution of the unsplit CN linear system, all intrinsic properties of the CNn method remain unchanged, including second-order temporal accuracy, time-reversal symmetry of the midpoint rule, unconditional stability for linear diffusion operators, and preservation of the dissipative structure of the parabolic problem. Consequently, the SPIM iteration preserves the algebraic structure of the unsplit CN formulation, while providing an efficient directional solver for the associated linear system.

The SPIM benchmark applies to both the heat subproblem (2.16)–(2.19) and the moisture subproblem (2.20)–(2.25). It may be interpreted as a Douglas–Rachford-type directional matrix-splitting iteration applied at the linear solver level rather than at the discretization level. Such line-iterative schemes originate from the classical ADI methods of Peaceman–Rachford [29] and Douglas [30]. Their convergence properties have been extensively analyzed within matrix-splitting theory [31] and modern operator-splitting frameworks [32]. Recent developments in diffusion–reaction splitting and matrix-splitting iteration methods further highlight the importance of stability preservation, error control, and efficient preconditioning strategies in diffusion-type partial differential equations and related multiphysics transport systems [33, 34]. In addition, modern structure-preserving operator-splitting schemes have been developed for reaction–diffusion systems to maintain the thermodynamic dissipation structure of the underlying equations; see, for example, Liu et al. [35]. Although the present heat and moisture diffusion model is linear and already exhibits dissipative behavior under the CN discretization, such structure-preserving approaches provide an important theoretical framework for constructing stable numerical methods for general diffusion systems.

Let $\mathbf{U}^n$ denote either $\mathbf{T}^{*,n}$ or $\mathbf{M}^{*,n}$ on the interior grid

$$\{\bar{u}_i\}_{i=1}^{N_u-1} \times \{\bar{v}_j\}_{j=1}^{N_v-1},$$

after enforcing the Robin boundary conditions by the ghost-point eliminations (2.29)–(2.31). Thus, the unknown vector contains only interior nodes, while the boundary contributions are embedded in the first and last rows of the reduced difference operators. Therefore, the matrix representation is constructed only on the interior unknowns. The boundary nodes are not excluded from the model; rather, their effect is incorporated through the modified first and last rows of the reduced difference matrices obtained after the Robin elimination. Consequently, the resulting linear system still represents the complete boundary-value problem but is written in reduced form with interior unknowns only.

Introduce the discrete directional Laplacians

$$(\delta_{\bar{u}\bar{u}}\mathbf{U})_{i,j} = \frac{U_{i+1,j} - 2U_{i,j} + U_{i-1,j}}{(\Delta\bar{u})^2}, \qquad (\delta_{\bar{v}\bar{v}}\mathbf{U})_{i,j} = \frac{U_{i,j+1} - 2U_{i,j} + U_{i,j-1}}{(\Delta\bar{v})^2},$$

and define

$$\mathcal{L}_{\bar{u}}(\mathbf{U}) = \delta_{\bar{u}\bar{u}}\mathbf{U}, \qquad \mathcal{L}_{\bar{v}}(\mathbf{U}) = \lambda^2\delta_{\bar{v}\bar{v}}\mathbf{U}, \qquad \mathcal{L} = \mathcal{L}_{\bar{u}} + \mathcal{L}_{\bar{v}}.$$

For the heat equation (2.16), because the Robin elimination (2.29) is nonhomogeneous, the reduced unsplit CN update takes the form

$$\Big(I - \frac{\Delta\bar{t}}{2}\mathcal{L}\Big)\mathbf{T}^{*,n+1} = \Big(I + \frac{\Delta\bar{t}}{2}\mathcal{L}\Big)\mathbf{T}^{*,n} + \mathbf{r}_{\mathcal{T}}, \tag{2.44}$$

where $\mathbf{r}_{\mathcal{T}}$ collects the constant contributions generated by the nonhomogeneous heat boundary condition $\mathcal{T}^* = 1$.

For the moisture equation (2.20), freezing the diffusivity coefficient $\mathcal{G}(\bar{t})$ during the time interval $[\bar{t}^n, \bar{t}^{n+1}]$ yields

$$\Big(I - \frac{\mathcal{G}^n\Delta\bar{t}}{2}\mathcal{L}\Big)\mathbf{M}^{*,n+1} = \Big(I + \frac{\mathcal{G}^n\Delta\bar{t}}{2}\mathcal{L}\Big)\mathbf{M}^{*,n}. \tag{2.45}$$

Both formulations can be written compactly as

$$\mathbf{A}_n\mathbf{U}^{n+1} = \mathbf{b}^n + \mathbf{r}^n,$$

where

$$\mathbf{A}_n = I - \frac{\mu_n\Delta\bar{t}}{2}\mathcal{L}, \qquad \mathbf{b}^n = \Big(I + \frac{\mu_n\Delta\bar{t}}{2}\mathcal{L}\Big)\mathbf{U}^n, \qquad \mu_n = \begin{cases} 1, & \mathbf{U} = \mathbf{T}^*, \\ \mathcal{G}^n, & \mathbf{U} = \mathbf{M}^*, \end{cases}$$

and

$$\mathbf{r}^n = \begin{cases} \mathbf{r}_{\mathcal{T}}, & \mathbf{U} = \mathbf{T}^*, \\ \mathbf{0}, & \mathbf{U} = \mathbf{M}^*. \end{cases}$$

For the moisture problem, $\mathcal{G}^n$ is frozen within each time step, so $\mathbf{A}_n$ remains fixed while solving for $\mathbf{U}^{n+1}$. Hence, although the coefficient $\mathcal{G}^n$ may vary from one time level to another, the matrix $\mathbf{A}_n$ and therefore the iteration matrix $\mathbf{B}_n$ remain fixed during the iterative solution process at each prescribed time level n.

Instead of solving the full two-dimensional sparse system directly, the SPIM computes $\mathbf{U}^{n+1}$ through the stationary iteration

$$r_{\bar{u}} = \frac{\mu_n\Delta\bar{t}}{2}, \qquad r_{\bar{v}} = \frac{\mu_n\lambda^2\Delta\bar{t}}{2}, \qquad \mathbf{U}^{(0)} = \mathbf{U}^n, \qquad \mathbf{R}^n = \Big(I + \frac{\mu_n\Delta\bar{t}}{2}\mathcal{L}\Big)\mathbf{U}^n + \mathbf{r}^n,$$

and, for $k = 0, 1, 2, \ldots$,

$$(I - r_{\bar{u}}\delta_{\bar{u}\bar{u}})\mathbf{U}^{(k+\frac{1}{2})} = \mathbf{R}^n + r_{\bar{v}}\delta_{\bar{v}\bar{v}}\mathbf{U}^{(k)}, \tag{2.46}$$

$$(I - r_{\bar{v}}\delta_{\bar{v}\bar{v}})\mathbf{U}^{(k+1)} = \mathbf{R}^n + r_{\bar{u}}\delta_{\bar{u}\bar{u}}\mathbf{U}^{(k+\frac{1}{2})}. \tag{2.47}$$

This symmetric splitting corresponds to a line Gauss–Seidel (Douglas–Rachford-type) iteration.

To rigorously justify convergence of the SPIM iteration, we now pass from the operator form to the matrix form of the reduced interior problem. After elimination of the Robin boundary nodes through (2.29)–(2.31), the unknown vector contains only the interior grid values, while the boundary conditions remain embedded in the first and last rows of the reduced matrices. Therefore, the resulting matrix system still represents the full boundary-value problem, written on the interior grid after Robin elimination.

Let $D_{\bar{u}} \in \mathbb{R}^{(N_u-1)\times(N_u-1)}$ and $D_{\bar{v}} \in \mathbb{R}^{(N_v-1)\times(N_v-1)}$ denote the reduced one-dimensional centered second-difference matrices in the $\bar{u}$- and $\bar{v}$-directions, respectively, including the modified first and last rows induced by the Robin boundary relations. More precisely, $D_{\bar{u}}$ has the form

$$D_{\bar{u}} = \frac{1}{(\Delta\bar{u})^2}\begin{bmatrix} -2+\eta_{\bar{u}}^{(L)} & 1 & 0 & \cdots & 0 \\ 1 & -2 & 1 & \ddots & \vdots \\ 0 & \ddots & \ddots & \ddots & 0 \\ \vdots & \ddots & 1 & -2 & 1 \\ 0 & \cdots & 0 & 1 & -2+\eta_{\bar{u}}^{(R)} \end{bmatrix},$$

and similarly

$$D_{\bar{v}} = \frac{1}{(\Delta\bar{v})^2}\begin{bmatrix} -2+\eta_{\bar{v}}^{(B)} & 1 & 0 & \cdots & 0 \\ 1 & -2 & 1 & \ddots & \vdots \\ 0 & \ddots & \ddots & \ddots & 0 \\ \vdots & \ddots & 1 & -2 & 1 \\ 0 & \cdots & 0 & 1 & -2+\eta_{\bar{v}}^{(T)} \end{bmatrix}.$$

For the heat problem, the Robin eliminations (2.29) give

$$U_{0,j} = \frac{1}{1+C_{T,u}}U_{1,j} + \frac{C_{T,u}}{1+C_{T,u}}, \qquad U_{N_u,j} = \frac{1}{1+C_{T,u}}U_{N_u-1,j} + \frac{C_{T,u}}{1+C_{T,u}},$$

and

$$U_{i,0} = \frac{1}{1+C_{T,v}}U_{i,1} + \frac{C_{T,v}}{1+C_{T,v}}, \qquad U_{i,N_v} = \frac{1}{1+C_{T,v}}U_{i,N_v-1} + \frac{C_{T,v}}{1+C_{T,v}}.$$

Therefore, in the heat case,

$$\eta_{\bar{u}}^{(L)} = \eta_{\bar{u}}^{(R)} = \frac{1}{1+C_{T,u}}, \qquad \eta_{\bar{v}}^{(B)} = \eta_{\bar{v}}^{(T)} = \frac{1}{1+C_{T,v}}.$$

The additional constant terms generated by the heat boundary elimination are absorbed into the right-hand-side vector and therefore do not alter the reduced diffusion matrices or the convergence analysis of the iteration matrix.

For the moisture problem, the Robin eliminations (2.31) give

$$U_{0,j} = \frac{1}{1+C_{M,u}^n}U_{1,j}, \qquad U_{N_u,j} = \frac{1}{1+C_{M,u}^n}U_{N_u-1,j},$$

and

$$U_{i,0} = \frac{1}{1+C_{M,v}^n}U_{i,1}, \qquad U_{i,N_v} = \frac{1}{1+C_{M,v}^n}U_{i,N_v-1}.$$

Hence, in the moisture case,

$$\eta_{\bar{u}}^{(L)} = \eta_{\bar{u}}^{(R)} = \frac{1}{1+C_{M,u}^n}, \qquad \eta_{\bar{v}}^{(B)} = \eta_{\bar{v}}^{(T)} = \frac{1}{1+C_{M,v}^n}.$$

Thus only the first and last diagonal entries differ from the standard centered second-difference matrix, while the interior stencil remains unchanged.

A real square matrix is called a *Z-matrix* if its off-diagonal entries are nonpositive, and a nonsingular *M-matrix* if it is a Z-matrix and its inverse is entrywise nonnegative. That is, if A is a nonsingular M-matrix, then $A^{-1} \geq 0$ entrywise. This means that every entry of A^{-1} is nonnegative; strict positivity is not required, so some entries may be equal to zero depending on the sparsity structure of the matrix.

Under the present Robin boundary conditions, $D_{\bar{u}}$ and $D_{\bar{v}}$ are symmetric negative definite matrices; hence $-D_{\bar{u}}$ and $-D_{\bar{v}}$ are symmetric positive definite Z-matrices and therefore nonsingular M-matrices.

Using Kronecker products, define the directional matrices

$$K = I_{N_v-1} \otimes D_{\bar{u}}, \qquad M = D_{\bar{v}} \otimes I_{N_u-1},$$

and define the full reduced two-dimensional diffusion matrix by

$$L = K + \lambda^2 M.$$

Here, M denotes the matrix associated with the $\bar{v}$-direction. Equivalently, K represents the discrete second-difference action in the $\bar{u}$-direction applied to all interior $\bar{v}$-lines, while M represents the discrete second-difference action in the $\bar{v}$-direction applied to all interior $\bar{u}$-lines. Therefore, L is exactly the full reduced matrix associated with the operator $\mathcal{L} = \mathcal{L}_{\bar{u}} + \mathcal{L}_{\bar{v}}$. Its block form is given by

$$L = \begin{bmatrix} D_{\bar{u}} + \lambda^2 d^{(\bar{v})}_{11} I & \lambda^2 d^{(\bar{v})}_{12} I & 0 & \cdots & 0 \\ \lambda^2 d^{(\bar{v})}_{21} I & D_{\bar{u}} + \lambda^2 d^{(\bar{v})}_{22} I & \lambda^2 d^{(\bar{v})}_{23} I & \ddots & \vdots \\ 0 & \ddots & \ddots & \ddots & 0 \\ \vdots & \ddots & \lambda^2 d^{(\bar{v})}_{N_v-2,N_v-3} I & D_{\bar{u}} + \lambda^2 d^{(\bar{v})}_{N_v-2,N_v-2} I & \lambda^2 d^{(\bar{v})}_{N_v-2,N_v-1} I \\ 0 & \cdots & 0 & \lambda^2 d^{(\bar{v})}_{N_v-1,N_v-2} I & D_{\bar{u}} + \lambda^2 d^{(\bar{v})}_{N_v-1,N_v-1} I \end{bmatrix},$$

where $d^{(\bar{v})}_{ij}$ denote the entries of $D_{\bar{v}}$ and each I is the identity matrix of order $N_u - 1$.

Accordingly, the matrix form of the unsplit CN system is

$$\mathbf{A}_n \mathbf{U}^{n+1} = \mathbf{b}^n + \mathbf{r}^n, \qquad \mathbf{A}_n = I - \frac{\mu_n \Delta\bar{t}}{2} L, \qquad \mathbf{b}^n = \Big(I + \frac{\mu_n \Delta\bar{t}}{2} L\Big)\mathbf{U}^n.$$

In matrix form, $\delta_{\bar{u}\bar{u}}$ and $\delta_{\bar{v}\bar{v}}$ correspond to K and M, respectively, so (2.46)–(2.47) become

$$(I - r_{\bar{u}} K)\mathbf{U}^{(k+\frac{1}{2})} = \mathbf{b}^n + \mathbf{r}^n + r_{\bar{v}} M \mathbf{U}^{(k)}, \qquad (I - r_{\bar{v}} M)\mathbf{U}^{(k+1)} = \mathbf{b}^n + \mathbf{r}^n + r_{\bar{u}} K \mathbf{U}^{(k+\frac{1}{2})}.$$

Eliminating $\mathbf{U}^{(k+\frac{1}{2})}$ yields

$$\mathbf{U}^{(k+1)} = \mathbf{B}_n \mathbf{U}^{(k)} + \mathbf{c}^n,$$

with

$$\mathbf{B}_n = (I - r_{\bar{v}} M)^{-1}(r_{\bar{u}} K)(I - r_{\bar{u}} K)^{-1}(r_{\bar{v}} M).$$

With the above matrix formulation in hand, we are now in a position to state the convergence result for the SPIM iteration.

Theorem 2.1. *For each fixed time level n, the SPIM iteration* (2.46)–(2.47) *converges to the unique solution of the unsplit CN system*

$$\mathbf{A}_n \mathbf{U}^{n+1} = \mathbf{b}^n + \mathbf{r}^n.$$

Moreover,

$$\rho(\mathbf{B}_n) < 1$$

for any mesh spacings $\Delta\bar{u} > 0$, $\Delta\bar{v} > 0$, *and any time step* $\Delta\bar{t} > 0$.

Proof. Because $D_{\bar{u}}$ and $D_{\bar{v}}$ are symmetric, so are K and M. Also,

$$KM = (I_{N_v-1} \otimes D_{\bar{u}})(D_{\bar{v}} \otimes I_{N_u-1}) = D_{\bar{v}} \otimes D_{\bar{u}} = MK,$$

so K and M commute and are simultaneously diagonalizable.

Let $\{\phi_p\}_{p=1}^{N_u-1}$ be an orthonormal eigenbasis of $-D_{\bar{u}}$ with eigenvalues $\alpha_p \geq 0$, and $\{\psi_q\}_{q=1}^{N_v-1}$ be an orthonormal eigenbasis of $-D_{\bar{v}}$ with eigenvalues $\beta_q \geq 0$, i.e.,

$$D_{\bar{u}}\phi_p = -\alpha_p\phi_p, \qquad D_{\bar{v}}\psi_q = -\beta_q\psi_q.$$

Under this ordering, the common eigenvectors are

$$\Phi_{pq} = \psi_q \otimes \phi_p,$$

and therefore

$$K\Phi_{pq} = -\alpha_p\Phi_{pq}, \qquad M\Phi_{pq} = -\beta_q\Phi_{pq}.$$

Applying $\mathbf{B}_n$ to Φ_{pq} gives

$$\mathbf{B}_n\Phi_{pq} = \frac{r_{\bar{u}}\alpha_p}{1 + r_{\bar{u}}\alpha_p}\,\frac{r_{\bar{v}}\beta_q}{1 + r_{\bar{v}}\beta_q}\,\Phi_{pq}.$$

Hence, the eigenvalues of $\mathbf{B}_n$ are

$$\theta_{pq}^{(n)} = \frac{r_{\bar{u}}\alpha_p}{1 + r_{\bar{u}}\alpha_p} \cdot \frac{r_{\bar{v}}\beta_q}{1 + r_{\bar{v}}\beta_q}, \qquad p = 1, \dots, N_u - 1, \quad q = 1, \dots, N_v - 1.$$

Since

$$r_{\bar{u}} > 0, \qquad r_{\bar{v}} > 0, \qquad \alpha_p \geq 0, \qquad \beta_q \geq 0,$$

each factor lies in $[0, 1)$, so

$$0 \leq \theta_{pq}^{(n)} < 1.$$

Thus,

$$\rho(\mathbf{B}_n) = \max_{p,q} \theta_{pq}^{(n)} < 1.$$

Let

$$\mathbf{e}^{(k)} = \mathbf{U}^{(k)} - \mathbf{U}^{n+1}$$

denote the iteration error. Since $\mathbf{U}^{n+1}$ is the fixed point of the iteration, we have

$$\mathbf{e}^{(k+1)} = \mathbf{B}_n\mathbf{e}^{(k)}.$$

Because $\rho(\mathbf{B}_n) < 1$, it follows that

$$\lim_{k\to\infty} \mathbf{e}^{(k)} = 0, \qquad \lim_{k\to\infty} \mathbf{U}^{(k)} = \mathbf{U}^{n+1}.$$

Equivalently, since $\mathbf{e}^{(k)} = \mathbf{B}_n^k\mathbf{e}^{(0)}$, the condition $\rho(\mathbf{B}_n) < 1$ implies

$$\lim_{k\to\infty} \mathbf{B}_n^k = 0,$$

and hence the iteration matrix converges to the zero matrix as the iteration count tends to infinity. Therefore, the SPIM iteration converges to the unique solution of the unsplit CN system for each fixed time level n. □

Algorithm 1. ADI–CN scheme for heat-moisture transfer

```
Input: $\lambda$, $\mathcal{D}_0$, $\mathcal{T}_i$, $\mathcal{T}_d$, $E_a/R$, $h$, $h_m$, $\mathcal{M}_d$; grid ($\mathcal{N}_\mathrm{u}$, $\mathcal{N}_\mathrm{v}$); time step $\Delta\bar{t}$; final time $\bar{t}_\mathrm{max}$.
Output: $\mathcal{T}^{*,n}_{i,j}$ and $\mathcal{M}^{*,n}_{i,j}$ for $0 \le \bar{t}^n \le \bar{t}_\mathrm{max}$.
Compute $\Delta\bar{u} = 1/\mathcal{N}_\mathrm{u}$ and $\Delta\bar{v} = 1/\mathcal{N}_\mathrm{v}$.
Initialize $\mathcal{T}^{*,0}_{i,j} = 0$ and $\mathcal{M}^{*,0}_{i,j} = 1$.
Set $n \leftarrow 0$ and $\bar{t}^0 \leftarrow 0$.
while $\bar{t}^n < \bar{t}_\mathrm{max}$ do
    Heat step (ADI–CN):
    Solve (2.34) for $\mathcal{T}^{*,n+\frac{1}{2}}$ (implicit in $\bar{u}$, explicit in $\bar{v}$).
    Update heat Robin boundaries using (2.29).
    Solve (2.36) for $\mathcal{T}^{*,n+1}$ (implicit in $\bar{v}$, explicit in $\bar{u}$).
    Update heat Robin boundaries using (2.29).
    Update moisture diffusivity:
    Compute $\overline{\mathcal{T}^{*}}(\bar{t}^n)$ using (2.27).
    Update $\mathcal{D}^n$ using (2.26).
    Set $\mathcal{G}^n \leftarrow \mathcal{D}^n/\alpha$.
    Moisture step (ADI–CN):
    Assemble the tridiagonal line systems with Robin elimination as in (2.40)–(2.43).
    Solve (2.38) for $\mathcal{M}^{*,n+\frac{1}{2}}$ using $\mathcal{G}^n$ (implicit in $\bar{u}$, explicit in $\bar{v}$).
    Update moisture Robin boundaries using (2.31).
    Solve (2.41) for $\mathcal{M}^{*,n+1}$ using $\mathcal{G}^n$ (implicit in $\bar{v}$, explicit in $\bar{u}$).
    Update moisture Robin boundaries using (2.31).
    $n \leftarrow n + 1$.
    $\bar{t}^n \leftarrow n\,\Delta\bar{t}$.
end while
```

3. Results and discussion

To verify the spatial convergence of the ADI–CN discretization, simulations were performed on refined grids of 31 × 25, 51 × 41, and 81 × 65. The dimensionless temperature at the geometric center and the maximum-norm difference between successive grid refinements were evaluated. The relative difference between the 51 × 41 and 81 × 65 solutions was below 10^{-4}, indicating grid-independent results. This confirms the expected second-order spatial accuracy of the central-difference discretization. The evolution of the dimensionless temperature field $\mathcal{T}^*(\mathrm{\bar{u}}, \mathrm{\bar{v}}, \mathrm{\bar{t}})$ was analyzed for a rectangular domain with physical dimensions $\mathcal{L} = 0.03$ m and $\mathcal{H} = 0.02$ m. The thermophysical properties were $k = 0.576$ W/(m K), $\rho = 856$ kg/m^3, and $c_p = 1929.72$ J/(kg K), yielding a thermal diffusivity $\alpha = 3.487 \times 10^{-7}$ m^2/s. Convective boundary conditions were imposed with a heat transfer coefficient $h = 250$ W/(m^2 K), an initial temperature $\mathcal{T}_i = 298$ K, and a drying-air temperature $\mathcal{T}_d = 323$ K.

At the physical time t = 100 s, as shown in Figure 1, the field $\mathcal{T}^*$ exhibits pronounced spatial nonuniformity. $\mathcal{T}^*$ approaches unity near the boundaries while remaining significantly lower in the interior. The temperature at the geometric center is about 307.4 K, while the temperature near the surfaces is about 322.0 K. The isotherms are closely spaced near the boundaries, indicating steep temperature gradients in these regions. This behavior indicates significant convective heating, which suggests the outermost layer reacts quickly while the heat slowly moves deeper into the material through conduction.

The temperature inside rises to about 315.3 K at $t = 200$ s. The difference in temperature between the center and the border decreases. The isotherms are coming together and moving apart, which means that the temperature differences are getting smaller. The height $\mathcal{H}$ distribution is more even because thermal fronts that start at the edges almost meet in the middle. Along the length $\mathcal{L}$, there are still different gradients. This is what Figure 2 shows.

At t = 300 s, the system goes into a late transient phase. The temperature range drops even more, from about 319.5 K to 322.7 K, so the inside is almost the same temperature. Figure 3 shows that the differences in internal temperature get smaller as the isotherms move farther apart. The height $\mathcal{H}$ doesn't change much, but there is still a small longitudinal gradient because $\mathcal{L}$ has a long diffusion distance. This behavior shows how the shape's aspect ratio and characteristic length scales change how heat moves over time.

Figure 4 shows that at t = 500 s, the temperature across the whole solid starts to even out. The temperature only changes between 322.3 K and 322.9 K, and the difference between the center and surface temperatures is less than 1 K. The maximum temperature gradient drops to about 8.0510^{1} K/m, which means that the force that drives internal conduction is almost gone. The solid is almost at thermal equilibrium with the air that is drying it out at this point. The rate of additional heating is much lower because the temperature difference is getting smaller. The temperature field exhibits the typical behavior of transient heat penetration into a solid during the early stage of convective heating. At first, heat only moves through thin layers near the edges, which are called internal thermal boundary layers. Over time, these layers become thicker at a rate that is about equal to $\sqrt{\alpha\, \mathrm{t}}$, where $\alpha = 3.487\times10^{-7}$ m^2/s is the thermal diffusivity. The penetration depth is very small compared to the characteristic dimensions $\mathcal{L}$ and $\mathcal{H}$ at first, which keeps the inside core relatively cold. The thermal fronts move toward the center over time until they meet. This makes the temperature differences inside slowly get smaller.

Due to the rectangular geometry, heat propagates through the height $\mathcal{H}$ more rapidly than through the length $\mathcal{L}$. Because of this, it takes less time for the thickness direction to reach a uniform temperature, but there are still temperature differences along the extended dimension. The Biot numbers in the $\bar{\mathrm{u}}$ and $\bar{\mathrm{v}}$ directions are 13.02 and 8.68, respectively. Both are much higher than 1. Because the Biot numbers are so high, heat transfer through convection at the surfaces is much stronger than heat transfer through conduction inside the object. The temperature on the surface quickly rises to the temperature of the drying air, $\mathcal{T}_d$, but the temperature inside rises more slowly. This is why the temperature differences were so big at first. It also shows that conduction within the solid is what makes it heat up. The high Biot numbers mean that the behavior is not lumped-capacitance and that a two-dimensional transient analysis is needed. As time goes on and the inside temperature rises, the difference in temperature between the solid and the air around it gets smaller. This slows down the rate of heat transfer, which helps the system reach a steady state.

The results show that a rectangular solid behaves as expected during transient convective heating: At first, strong convection quickly raises the surface temperature; then, diffusion warms the inside; and finally, the temperature distribution becomes more even across the solid. The isotherms change smoothly, and the temperature profiles converge steadily, which shows that the proposed ADI–CN scheme is correct and strong.

The ADI–CN scheme with convective (Robin) boundary conditions on all sides is also used to model how moisture moves through the rectangular solid over time. The air that is drying has a moisture content of 0.196 g/g (dry basis), and the convective mass transfer coefficient is 10^{-4} m/s. We run all of the simulations on a spatial grid that is 51×41 and has a time step of 0.1 seconds. We select the effective moisture diffusivity $\mathcal{D}(\mathrm{t})$ and the appropriate ADI coefficients to ensure stability and precision in time integration.

Figures 5–8 show how the moisture level changes over time as the drying process goes on. At $\mathrm{t} = 100$ s, Figure 5 shows that the moisture distribution is very uneven. This is because convective effects cause a lot of moisture to move from the center to the surface. The inside, on the other hand, stays very moist. The moisture content goes from a steady value to a range of 1.17 to 2.94 g/g. This shows that the core is much wetter than the surfaces that are drying.

Figure 6 shows that drying for a longer time at $\mathrm{t} = 200$ s lowers the moisture range even more, bringing it down to about 0.48–1.83 g/g. The moisture contours become more closely spaced, and the differences between the inside and outside surfaces are less clear than they were at first. This corresponds to the classical falling-rate drying period, during which internal diffusion becomes the dominant transport mechanism. Figure 7 shows that by $\mathrm{t} = 300$ s, the moisture distribution becomes significantly more uniform. Figure 8 shows that at the last stage, $\mathrm{t} = 500$ s, the moisture field is almost the same all over the object, with values between 0.215 and 0.305 g/g. Overall, Figures 5–8 illustrate the convective drying behavior of porous rectangular solids.

A comparative study between the ADI–CN scheme and an unsplit CN formulation solved via an SPIM was conducted for both the two-dimensional heat and moisture diffusion subproblems on a 51×41 grid with $\Delta t = 0.1$ and $t = 300$, as shown in Figures 9 and 10, respectively. For the heat equation, the computational time required by the ADI–CN scheme was 0.639 seconds, whereas the SPIM–CN implementation required 1.560 seconds, yielding a time ratio of 2.44. The discrepancy between the two numerical solutions remains extremely small: The infinity norm of the difference is 3.05×10^{-7} and the relative L_2 difference is 5.52×10^{-10}. These results demonstrate that the ADI splitting preserves the accuracy of the underlying CN discretization to near-machine precision for the heat subproblem, while maintaining superior computational efficiency.

For the moisture diffusion equation with Arrhenius-type diffusivity, the ADI–CN scheme required 5.113 seconds, while the SPIM–CN implementation required 1.655 seconds, corresponding to a time ratio of 0.324. The discrepancy norms are still small in this case: The infinity norm of the difference is 1.65×10^{-3} and the relative L_2 difference is 1.89×10^{-3}. The moisture problem involves temperature-dependent diffusivity and Robin boundary conditions. However, the splitting error caused by the ADI formulation stays under control and does not affect second-order accuracy.

The average number of SPIM iterations per time step is about 2 for both subproblems (about 2.01 for heat and 2.03 for moisture). This shows that the fixed-point method is quickly converging to the unsplit CN solution. In general, these results show that the suggested ADI–CN scheme is just as accurate as an unsplit CN discretization and is still fast enough to solve two-dimensional diffusion problems. The very small discrepancy norms further confirm that the operator splitting does not make the underlying second-order discretization less stable or consistent. Figures 11 and 12 show the differences between experimental data, analytical solutions, and the proposed numerical scheme for both heat and moisture distributions. The results demonstrate a significant alignment between the experimental observations and the analytical models. The current formulation accommodates variable material properties; however, the constant-coefficient scenario was selected to facilitate a coherent and significant comparison with both analytical and experimental outcomes, where the experimental data utilized for validation pertain to the convective drying of rectangular apple slabs.

The first stage of drying is characterized by a convection-dominated regime, which means that heat and mass transfer at the surface are the most important things happening during this stage. Near the edges, the temperature and humidity change quickly, but the inside stays pretty much the same. This stage is the same as the normal drying period at a constant rate. The main thing that happens during drying is that the moisture inside the material moves around. The surface moisture content decreases progressively, and the gradients slowly move toward the middle. This behavior starts the falling-rate period, when drying proceeds more slowly due to internal diffusion resistance. The simulated temperature and moisture fields clearly illustrate the transition from surface-controlled transport to diffusion-controlled internal transport. All numerical simulations were performed using MATLAB R2023b.

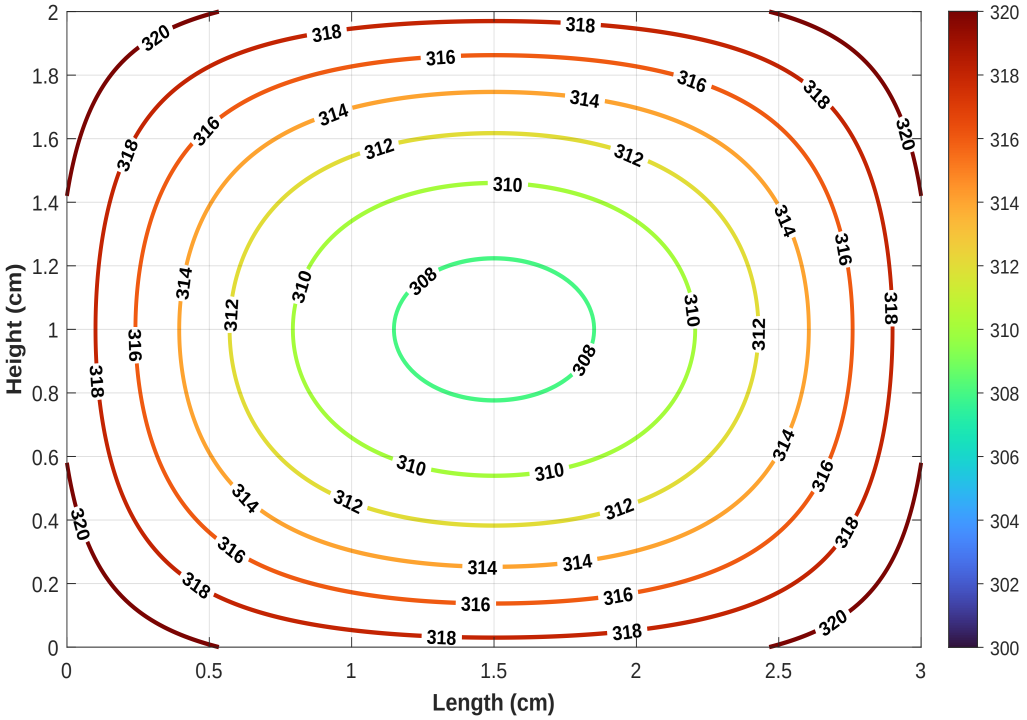

Figure 1. Temperature distribution at t = 100 s within a rectangular object using the ADI–CN scheme.

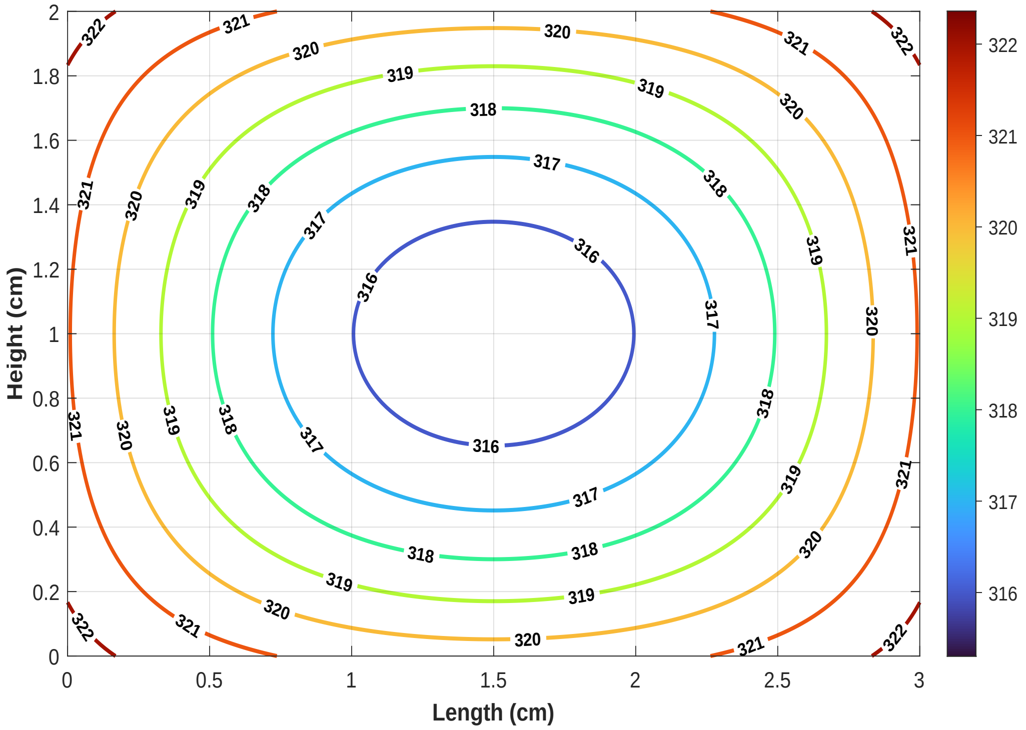

Figure 2. Temperature distribution at t = 200 s within a rectangular object using the ADI–CN scheme.

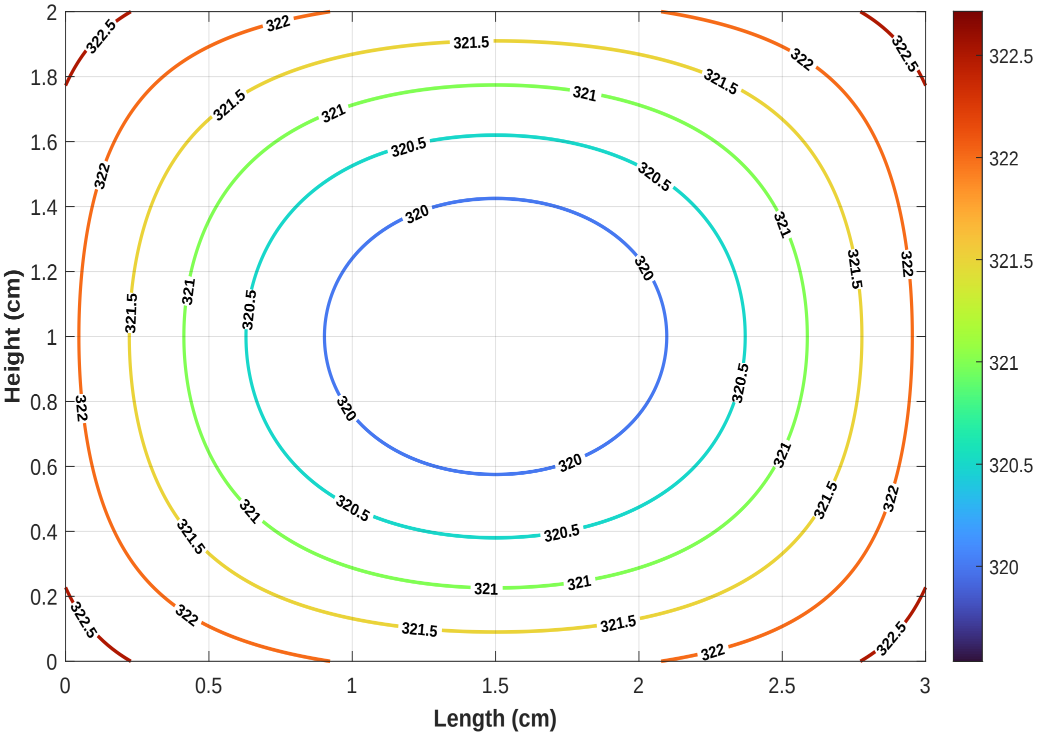

Figure 3. Temperature distribution at t = 300 s within a rectangular object using the ADI–CN scheme.

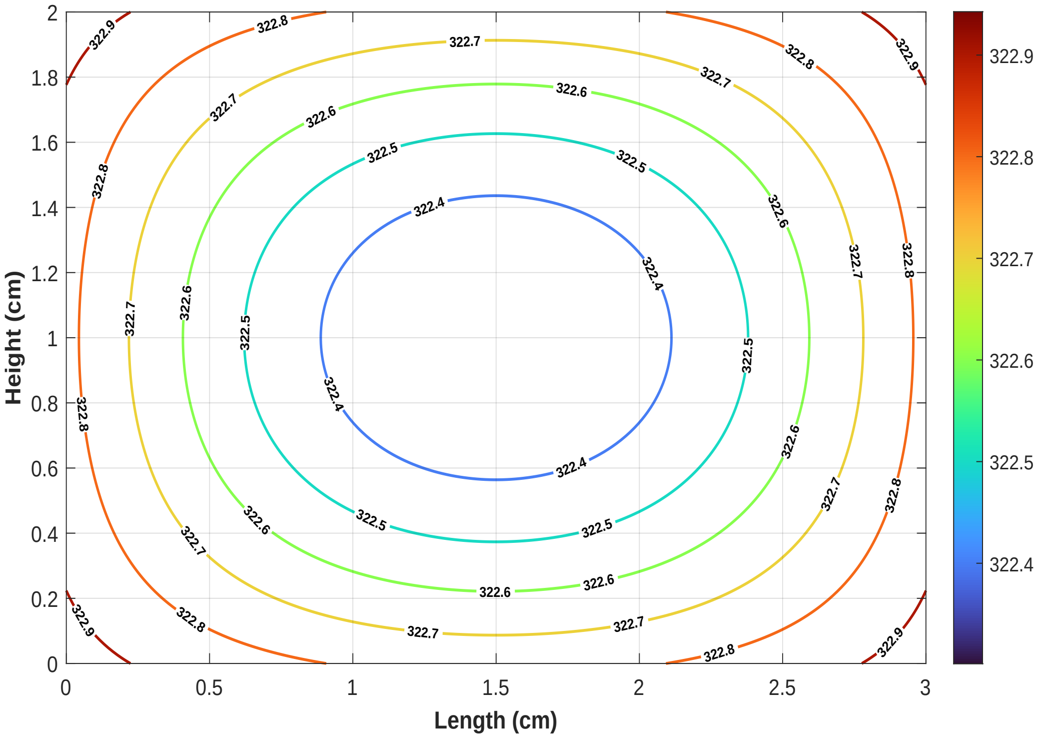

Figure 4. Temperature distribution at t = 500 s within a rectangular object using the ADI–CN scheme.

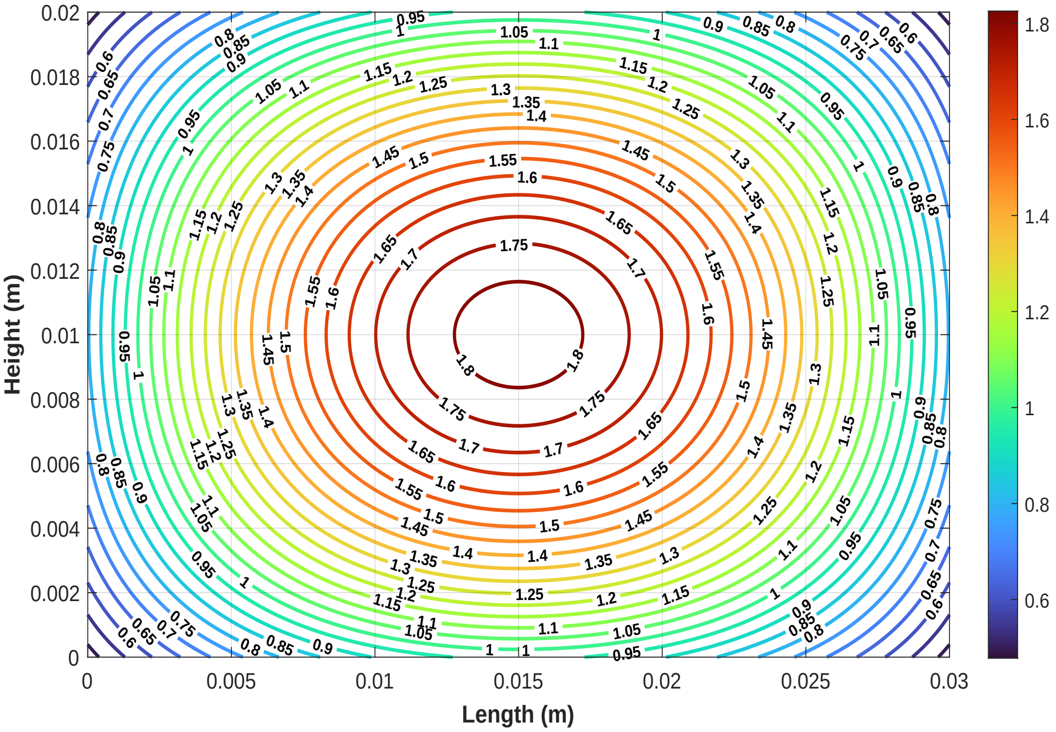

Figure 5. Moisture distribution at t = 100 s within a rectangular object using the ADI–CN scheme.

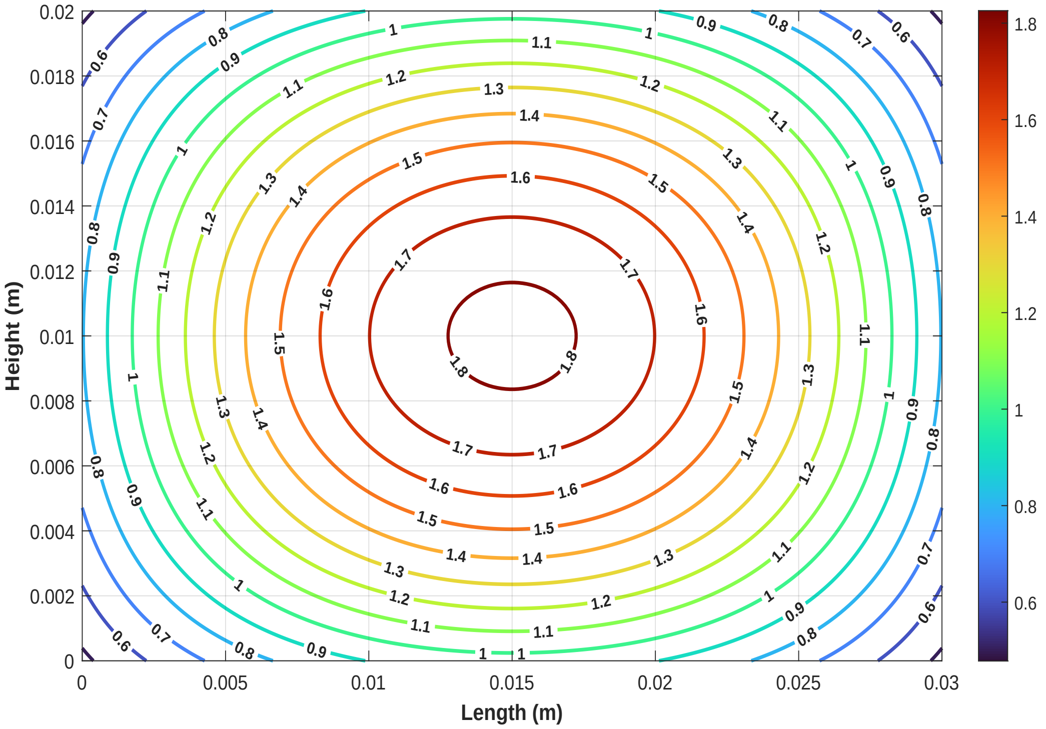

Figure 6. Moisture distribution at t = 200 s within a rectangular object using the ADI–CN scheme.

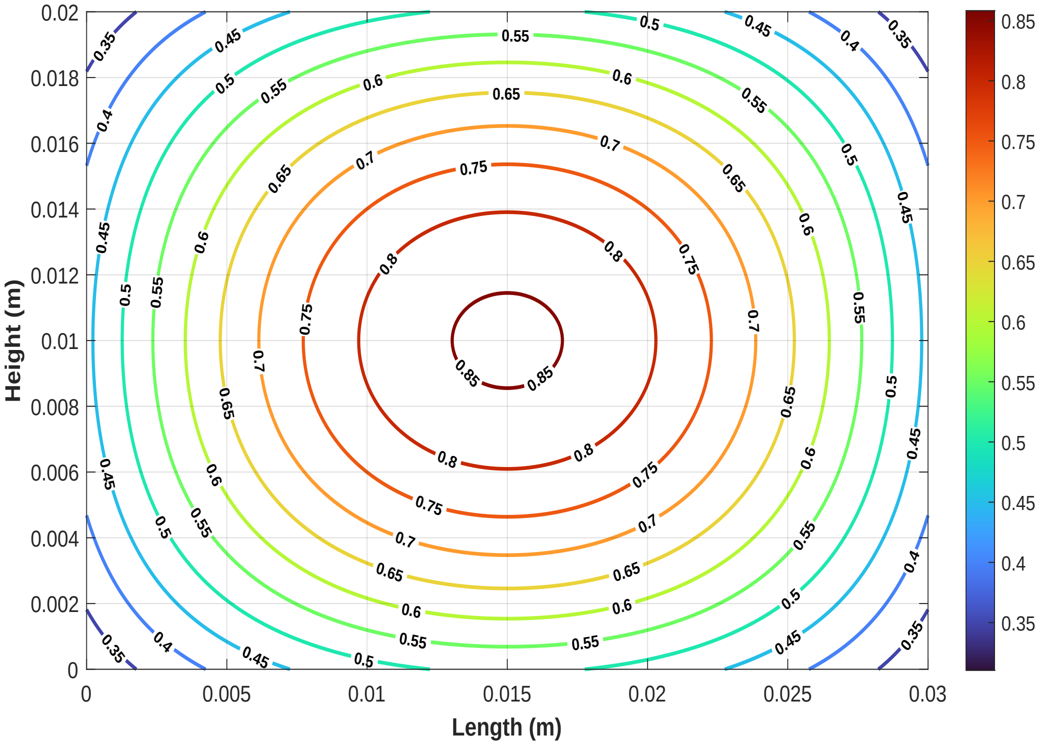

Figure 7. Moisture distribution at t = 300 s within a rectangular object using the ADI–CN scheme.

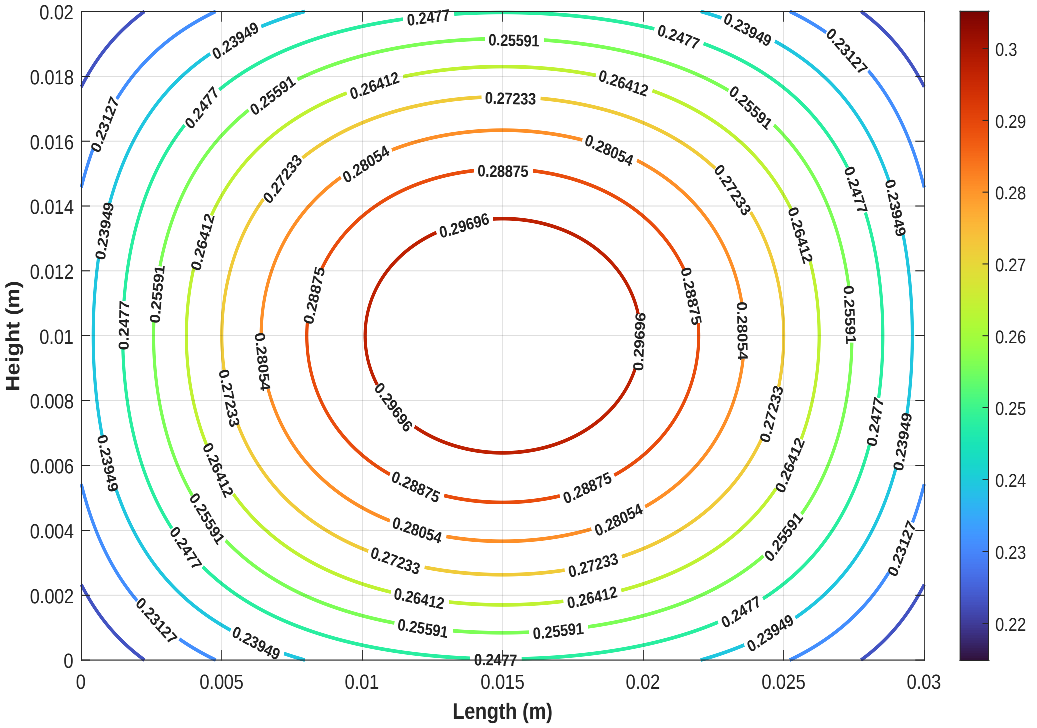

Figure 8. Moisture distribution at t = 500 s within a rectangular object using the ADI–CN scheme.

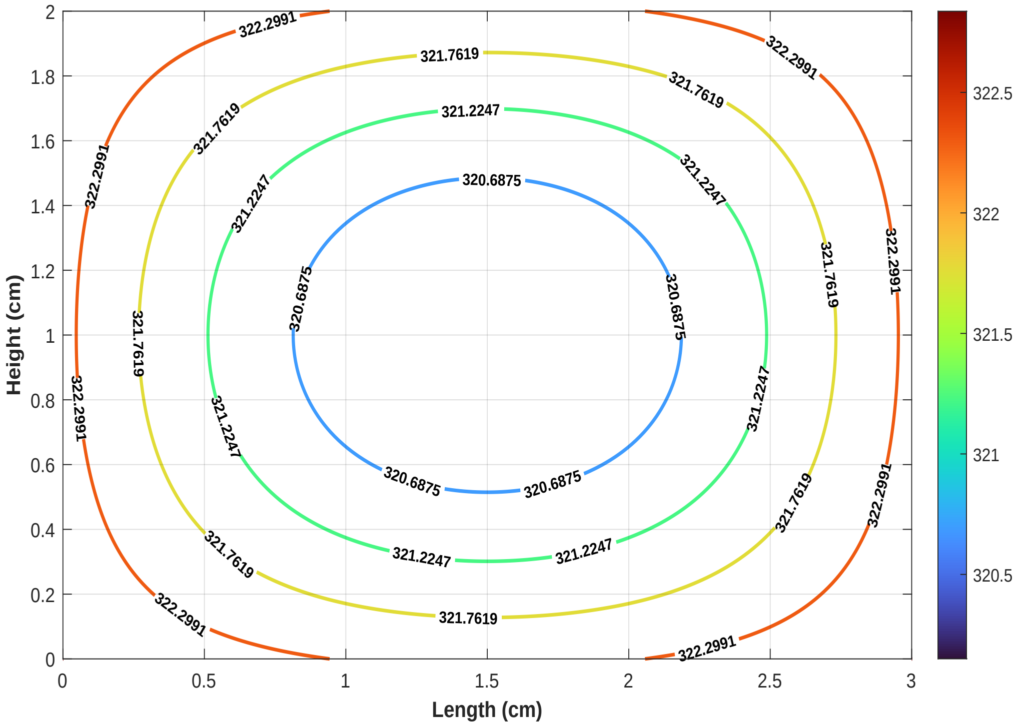

Figure 9. Temperature distribution at t = 300 s within a rectangular object using the SPIM–CN scheme.

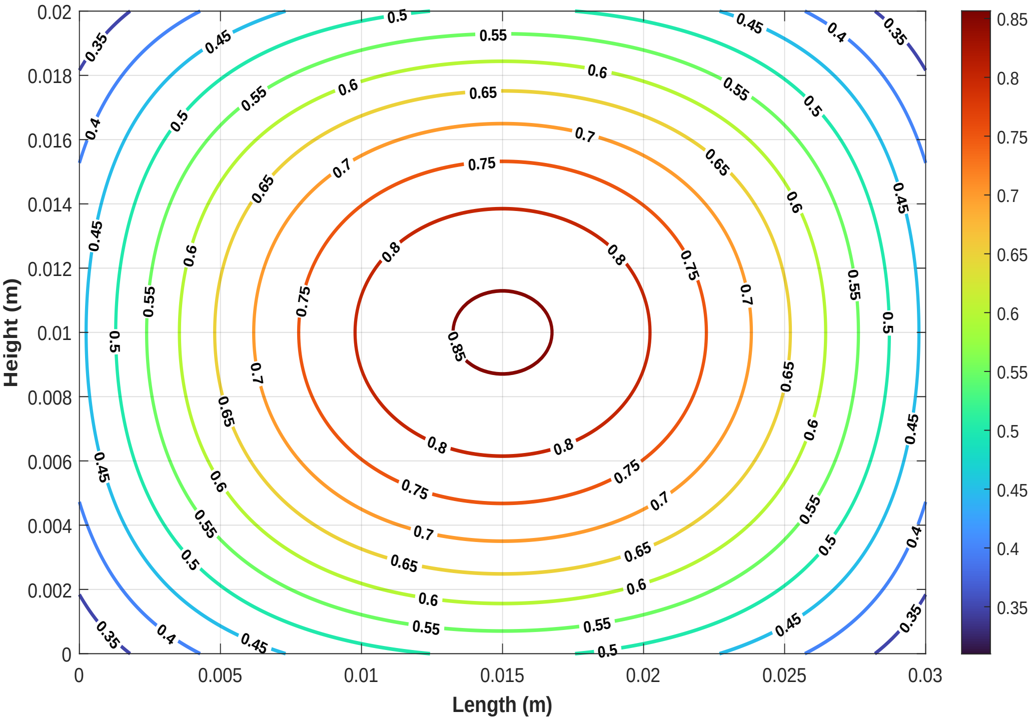

Figure 10. Moisture distribution at t = 300 s within a rectangular object using the SPIM–CN scheme.

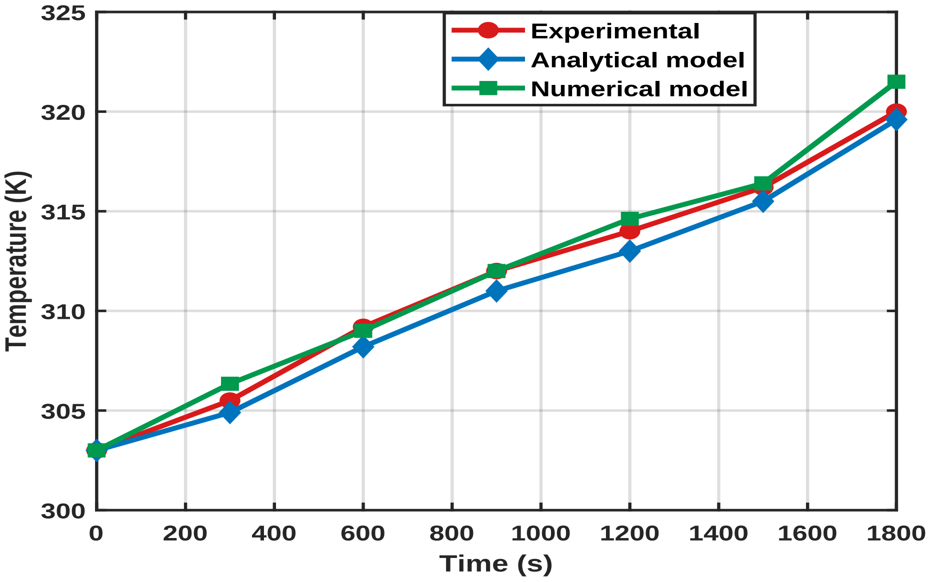

Figure 11. Comparison of measured and predicted center temperatures in a rectangular object.

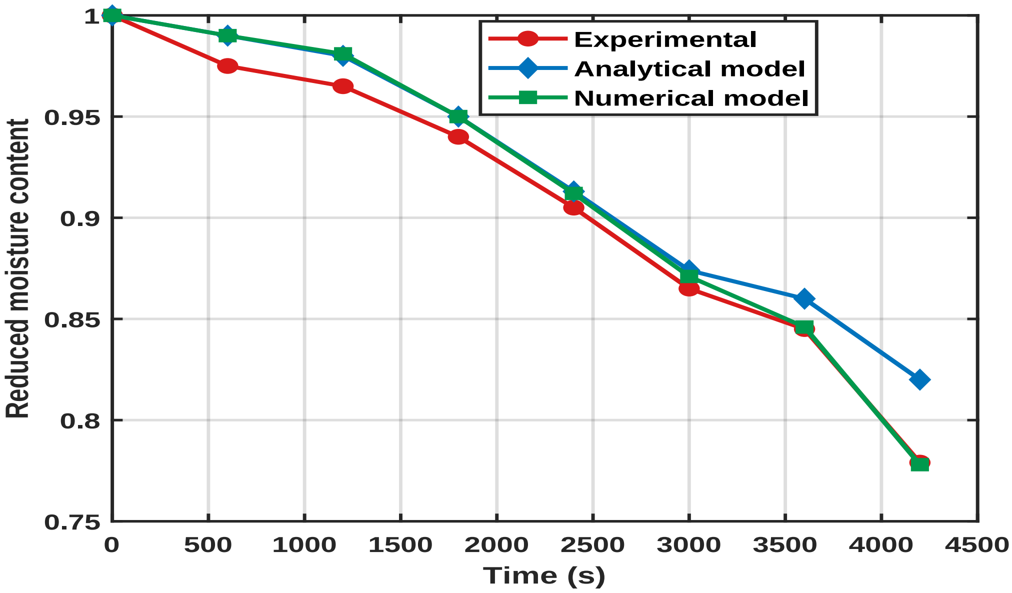

Figure 12. Comparison of measured and predicted moisture content distributions in a rectangular object.

4. Conclusions

In this study, a two-dimensional model for transient heat and moisture transfer in a rectangular domain under convective drying has been developed and analyzed. The governing diffusion equations, derived from Fourier's and Fick's laws, were nondimensionalized and discretized using central finite differences in space and a CN time scheme combined with a Peaceman–Rachford ADI splitting strategy. The resulting method is second-order accurate in time and space and unconditionally stable for linear diffusion operators. Numerical simulations show how things usually dry: The temperature rises quickly at first, then levels off slowly, and the moisture drops quickly at first, then decreases slowly. The obtained temperature and moisture fields match exceptionally well with existing analytical solutions and experimental data. Also, we compare the ADI–CN method to an unsplit CN formulation solved with an SPIM. The numerical results demonstrate that the proposed ADI–CN scheme maintains accuracy comparable to the SPIM–CN method while retaining competitive computational efficiency across the tested scenarios. In general, the proposed framework is a reliable and accurate way to model how heat and moisture move through rectangular food products. Future work will incorporate temperature and moisture-sensitive properties and shrinkage effects via moving-boundary and thermo-mechanical coupling formulations.

Use of Generative-AI tools declaration

The author declares he has not used Artificial Intelligence (AI) tools in the creation of this article.

Funding

This work was supported by the Deanship of Scientific Research, Vice Presidency for Graduate Studies and Scientific Research, King Faisal University, Saudi Arabia [Grant No. KFU261545].

Conflict of interest

The author declares no conflicts of interest.

References

1. A. S. Mujumdar, *Handbook of industrial drying*, 4 Eds., CRC Press, Boca Raton, FL, 2014. https://doi.org/10.1201/b17208
2. I. Dincer, S. Dost, A modelling study for moisture diffusivities and moisture transfer coefficients in drying of solid objects, *Int. J. Energy Res.*, **20** (1996), 531–539. https://doi.org/10.1002/(SICI)1099-114X(199606)20:6¡531::AID-ER171¿3.0.CO;2-6
3. F. Nadi, G. H. Rahimi, R. Younsi, T. Tavakoli, Z. Hamidi-Esfahani, Numerical simulation of vacuum drying by Luikov's equations, *Dry. Technol.*, **30** (2012), 197–206. https://doi.org/10.1080/07373937.2011.595860
4. W. C. Chiang, J. N. Petersen, Experimental measurement of temperature and moisture profiles during apple drying, *Dry. Technol.*, **5** (1987), 25–49. https://doi.org/10.1080/07373938708916527
5. A. A. Uglov, V. F. Brekhovskikh, Temperature field in a two-layer plate heated by a surface source, *J. Eng. Phys.*, **10** (1966), 305–306. https://doi.org/10.1007/BF00837830
6. M. M. Hussain, I. Dincer, Numerical simulation of two-dimensional heat and moisture transfer during drying of a rectangular object, *Numer. Heat Transf. A*, **43** (2003), 867–878. https://doi.org/10.1080/713838150
7. A. Kaya, O. Aydin, I. Dincer, Numerical modeling of heat and mass transfer during forced convection drying of rectangular moist objects, *Int. J. Heat Mass Transf.*, **49** (2006), 3094–3103. https://doi.org/10.1016/j.ijheatmasstransfer.2006.01.043
8. M. A. Ruiz-Cabrera, M. A. Salgado-Cervantes, K. N. Walislewski-Kubiak, M. A. García-Alvarado, The effect of path diffusion on the effective moisture diffusivity in carrot slabs, *Dry. Technol.*, **15** (1997), 169–181. https://doi.org/10.1080/07373939708917224
9. T. Akiyama, H. Liu, K. I. Hayakawa, Hygrostress-multicrack formation and propagation in cylindrical viscoelastic food undergoing heat and moisture transfer processes, *Int. J. Heat Mass Transf.*, **40** (1997), 1601–1609. https://doi.org/10.1016/S0017-9310(96)00206-2
10. J. A. Rogers, M. Kaviany, Variation of heat and mass transfer coefficients during drying of granular beds, *ASME J. Heat Transf.*, **112** (1990), 668–674. https://doi.org/10.1115/1.2910439
11. P. Perre, M. Moser, M. Martin, Advances in transport phenomena during convective drying with superheated steam and moist air, *Int. J. Heat Mass Transf.*, **36** (1993), 2725–2746. https://doi.org/10.1016/0017-9310(93)90093-L

12. S. H. Sun, T. R. Marrero, Experimental study of simultaneous heat and moisture transfer around single short porous cylinders during convection drying by a psychrometry method, *Int. J. Heat Mass Transf.*, **39** (1996), 3559–3565. https://doi.org/10.1016/0017-9310(96)00045-2

13. I. Dincer, S. Dost, Determination of moisture diffusivities and moisture transfer coefficients for wooden slabs subject to drying, *Wood Sci. Technol.*, **30** (1996), 245–251. https://doi.org/10.1007/BF00229347

14. L. Villa-Corrales, J. J. Flores-Prieto, J. P. Xamán-Villaseñor, E. García-Hernández, Numerical and experimental analysis of heat and moisture transfer during drying of Ataulfo mango, *J. Food Eng.*, **98** (2010), 198–206. https://doi.org/10.1016/j.jfoodeng.2009.12.026

15. Y. Li, M. Liang, J. Li, K. Jiang, X. Li, Z. Zheng, Simulation and experimental studies of heat-mass transfer and stress–strain in carrots during hot air drying, *Agriculture*, **15** (2025), 484. https://doi.org/10.3390/agriculture15050484

16. I. Selmer, P. Farrell, I. Smirnova, P. Gurikov, Comparison of finite difference and finite volume simulations for a sc-drying mass transport model, *Gels*, **6** (2020), 45. https://doi.org/10.3390/gels6040045

17. C. Lamnatou, E. Papanicolaou, V. Belessiotis, N. Kyriakis, Finite-volume modelling of heat and mass transfer during convective drying of porous bodies–non-conjugate and conjugate formulations involving the aerodynamic effects, *Renew. Energ.*, **35** (2010), 1391–1402. https://doi.org/10.1016/j.renene.2009.11.008

18. A. Szpicer, W. Bińkowska, A. Stelmasiak, I. Wojtasik-Kalinowska, A. Czajkowska, S. Mierzejewska, et al., Advances in computational fluid dynamics of mechanical processes in food engineering: Mixing, extrusion, drying, and process optimization, *Appl. Sci.*, **15** (2025), 8752. https://doi.org/10.3390/app15158752

19. M. I. H. Khan, Z. Welsh, Y. Gu, M. A. Karim, B. Bhandari, Modelling of simultaneous heat and mass transfer considering the spatial distribution of air velocity during intermittent microwave convective drying, *Int. J. Heat Mass Transf.*, **153** (2020), 119668. https://doi.org/10.1016/j.ijheatmasstransfer.2020.119668

20. A. Szpicer, W. Bińkowska, I. Wojtasik-Kalinowska, S. M. Salih, A. Półtorak, Application of computational fluid dynamics simulations in food industry, *Eur. Food Res. Technol.*, **249** (2023), 1411–1430. https://doi.org/10.1007/s00217-023-04231-y

21. W. J. Ferguson, R. W. Lewis, L. Tömösy, A finite element analysis of freeze-drying of a coffee sample, *Comput. Method. Appl. Mech. Eng.*, **108** (1993), 341–352. https://doi.org/10.1016/0045-7825(93)90009-M

22. F. Selimefendigil, S. Ö. Çoban, H. F. Öztop, Investigation of time dependent heat and mass transportation for drying of 3D porous moist objects in convective conditions, *Int. J. Therm. Sci.*, **162** (2021), 106788. https://doi.org/10.1016/j.ijthermalsci.2020.106788

23. J. T. Teleken, S. M. Amorim, S. S. S. Rodrigues, T. W. P. de Souza, J. P. Ferreira, B. A. M. Carciofi, Heat and mass transfer in shrimp hot-air drying: Experimental evaluation and numerical simulation, *Foods*, **14** (2025), 428. https://doi.org/10.3390/foods14030428

24. J. Irudayaraj, K. Haghighi, R. L. Stroshine, Nonlinear finite element analysis of coupled heat and mass transfer problems with an application to timber drying, *Dry. Technol.*, **8** (1990), 731–749. https://doi.org/10.1080/07373939008959912

25. P. Jayapragasam, P. Le Bideau, T. Loulou, Luikov's analytical solution with complex eigenvalues in intensive drying, *Transport Porous Med.*, **130** (2019), 923–946. https://doi.org/10.1007/s11242-019-01348-1

26. V. A. Sychevskii, Heat and mass transfer in convective wood-drying plants, *J. Eng. Phys. Thermophys.*, **91** (2018), 705–711. https://doi.org/10.1007/s10891-018-1793-0

27. Y. Yang, G. Rzadkowski, A. Pasban, E. Tohidi, S. Shateyi, A high accurate scheme for numerical simulation of two-dimensional mass transfer processes in food engineering, *Alex. Eng. J.*, **60** (2021), 2629–2639. https://doi.org/10.1016/j.aej.2020.12.055

28. N. P. Zogzas, Z. B. Maroulis, Effective moisture diffusivity estimation from drying data: A comparison between various methods of analysis, *Dry. Technol.*, **14** (1996), 1543–1573. https://doi.org/10.1080/07373939608917163

29. D. W. Peaceman, H. H. Rachford, Jr., The numerical solution of parabolic and elliptic differential equations, *J. Soc. Ind. Appl. Math.*, **3** (1955), 28–41. https://doi.org/10.1137/0103003

30. J. Douglas, Jr., On the numerical integration of $u_{xx}+u_{yy}=u_t$ by implicit methods, *J. Soc. Ind. Appl. Math.*, **3** (1956), 42–65.

31. R. S. Varga, *Matrix iterative analysis*, Springer Series in Computational Mathematics, Springer, Heidelberg, **27** (2009).

32. S. Blanes, F. Casas, A. Murua, Splitting methods for differential equations, *Acta Numer.*, **33** (2024), 1–161. https://doi.org/10.1017/S0962492923000077

33. L. Einkemmer, A. Ostermann, Overcoming order reduction in diffusion-reaction splitting. Part 1: Dirichlet boundary conditions, *SIAM J. Sci. Comput.*, **37** (2015), A1577–A1592. https://doi.org/10.1137/140994204

34. W. Hundsdorfer, J. G. Verwer, *Numerical solution of time-dependent advection-diffusion-reaction equations*, Springer Series in Computational Mathematics, Springer, Berlin, 2003. https://doi.org/10.1007/978-3-662-09017-6

35. C. Liu, C. Wang, Y. Wang, A structure-preserving, operator splitting scheme for reaction-diffusion equations with detailed balance, *J. Comput. Phys.*, **436** (2021), 110253. https://doi.org/10.1016/j.jcp.2021.110253

AIMS Press